

# Supplementary note on diffractive analyses of 2015 proton-proton data:

- [1] Measurement of Central Exclusive Production of  $h\bar{h}$  pairs  $(h=\pi,K,p)$  with Roman Pot detectors in diffractive proton-proton interactions at  $\sqrt{s}=200~{\rm GeV}$
- [2] Measurement of particle production with Roman Pot detectors in diffractive proton-proton interactions at  $\sqrt{s} = 200 \text{ GeV}$

Leszek Adamczyk<sup>1</sup>, Łukasz Fulek<sup>1</sup>, and Rafał Sikora<sup>1</sup>

<sup>1</sup>AGH University of Science and Technology, FPACS, Kraków, Poland

June 11, 2018

#### Abstract

In this note we present supplementary material related to analyses of diffractive processes based on 2015 data from proton-proton collisions at  $\sqrt{s}=200$  GeV. This dataset was collected with newly installed Roman Pot detectors in Phase II\* configuration which ensured efficient triggering and measuring diffractively scattered protons.

We focus on calculation of efficiencies, corrections to Monte Carlo simulations and derivation of systematic uncertainties of our measurements.

## Contents

1	Efficiencies	3
	1.1 TPC track acceptance and reconstruction efficiency	3
	1.2 TOF acceptance, hit reconstruction and track-matching efficiency	16
	1.3 TPC vertex reconstruction efficiency	29
2	Roman Pot simulation	30
3	$\mathrm{d}E/\mathrm{d}x$ correction	31
4	TPC track pointing resolution adjustment	35
5	Dead material in front of TPC	38
6	Systematic errors	43
Li	ist of Figures	45
Li	ist of Tables	45
$\mathbf{R}$	eferences	46

#### 1. Efficiencies

#### 1.1 TPC track acceptance and reconstruction efficiency

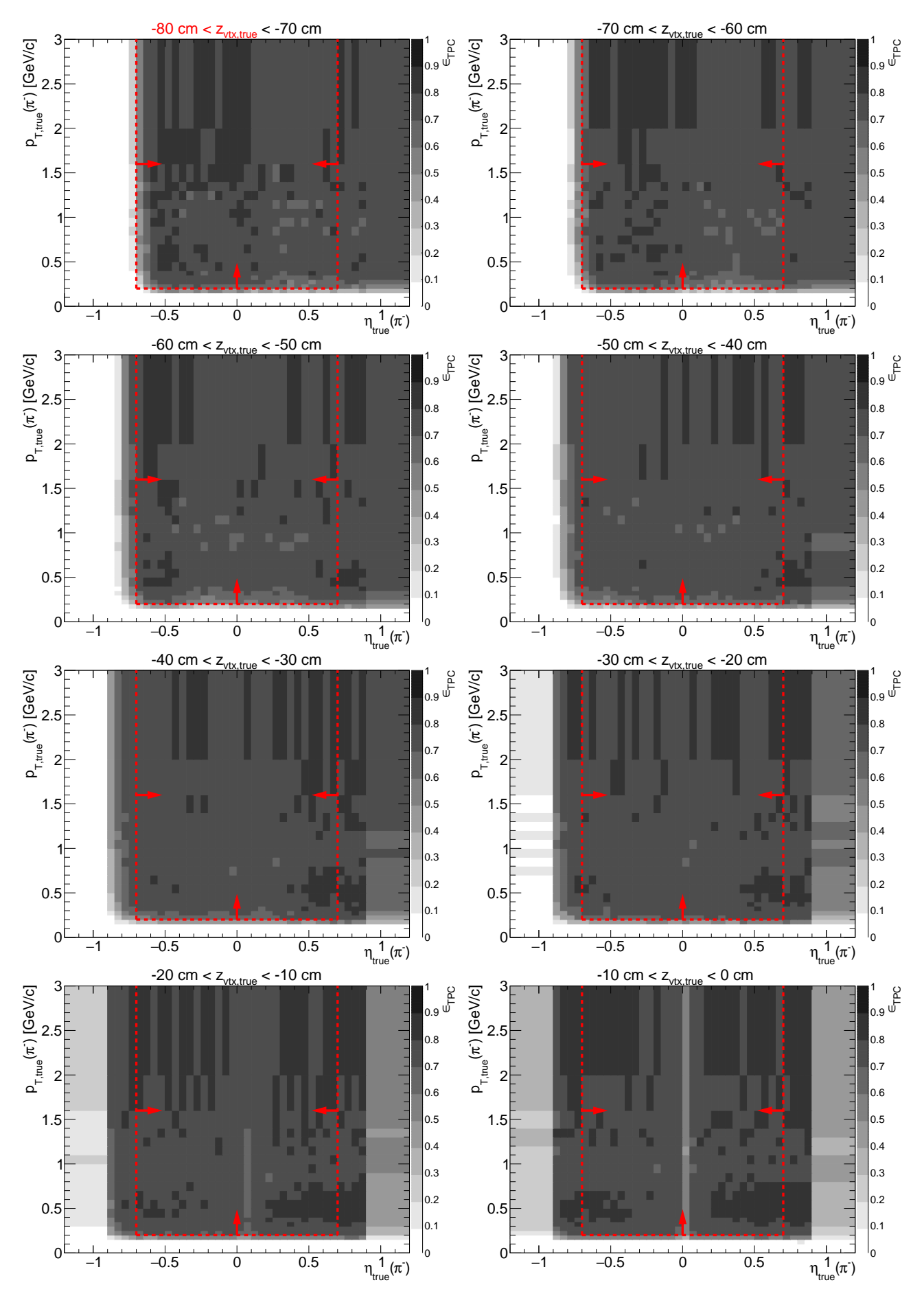
We define joint acceptance and efficiency of the reconstruction of a track in the TPC,  $\epsilon_{\text{TPC}}$ , as the probability that particle from the primary interaction generates signal in the detector which is reconstructed as a track that satisfies all quality criteria and whose  $p_T$  and  $\eta$  are within the kinematic region of the measurement (cuts ?? and ??).

The chnically this quantity is derived from STARsim MC embedded into zero-bias triggers in the following procedure:

- 1. True-level primary particles of given ID and charge, with all physics  $(p_T^{\text{true}}, \eta^{\text{true}})$  and detector  $(z_{\text{vx}})$  quantities within defined region of the measurement, are selected (set A).
- 2. Each particle from set A is checked if global TPC track with more than half of hit points generated by this particle, was reconstructed. All global tracks which are associated with true-level primary particles and satisfy kinematic and quality criteria (cuts ?? and ??), form set B.
- 3. The joint TPC acceptance and efficiency is calculated as the ratio of the histograms of true-level quantities (such as  $p_T$ ,  $\eta$ ,  $z_{vx}$ ) for particles from set B and particles from set A:

$$\epsilon_{\text{TPC}}(p_T, \eta, z_{vx}; \text{ sign, PID}) = \frac{(p_T, \eta, z_{vx}) \text{ histogram for particles of given sign and ID from } set B}{(p_T, \eta, z_{vx}) \text{ histogram for particles of given sign and ID from } set A}. (1.1)$$

Figure 1.1: TPC acceptance and reconstruction efficiency of  $\pi^-$ . Each plot represents the TPC efficiency  $\epsilon_{\text{TPC}}$  (z-axis) as a function of true particle pseudorapidity  $\eta$  (x-axis) and transverse momentum  $p_T$  (y-axis) in single z-vertex bin whose range is given at the top. Red lines and arrows indicate region accepted in analyses.



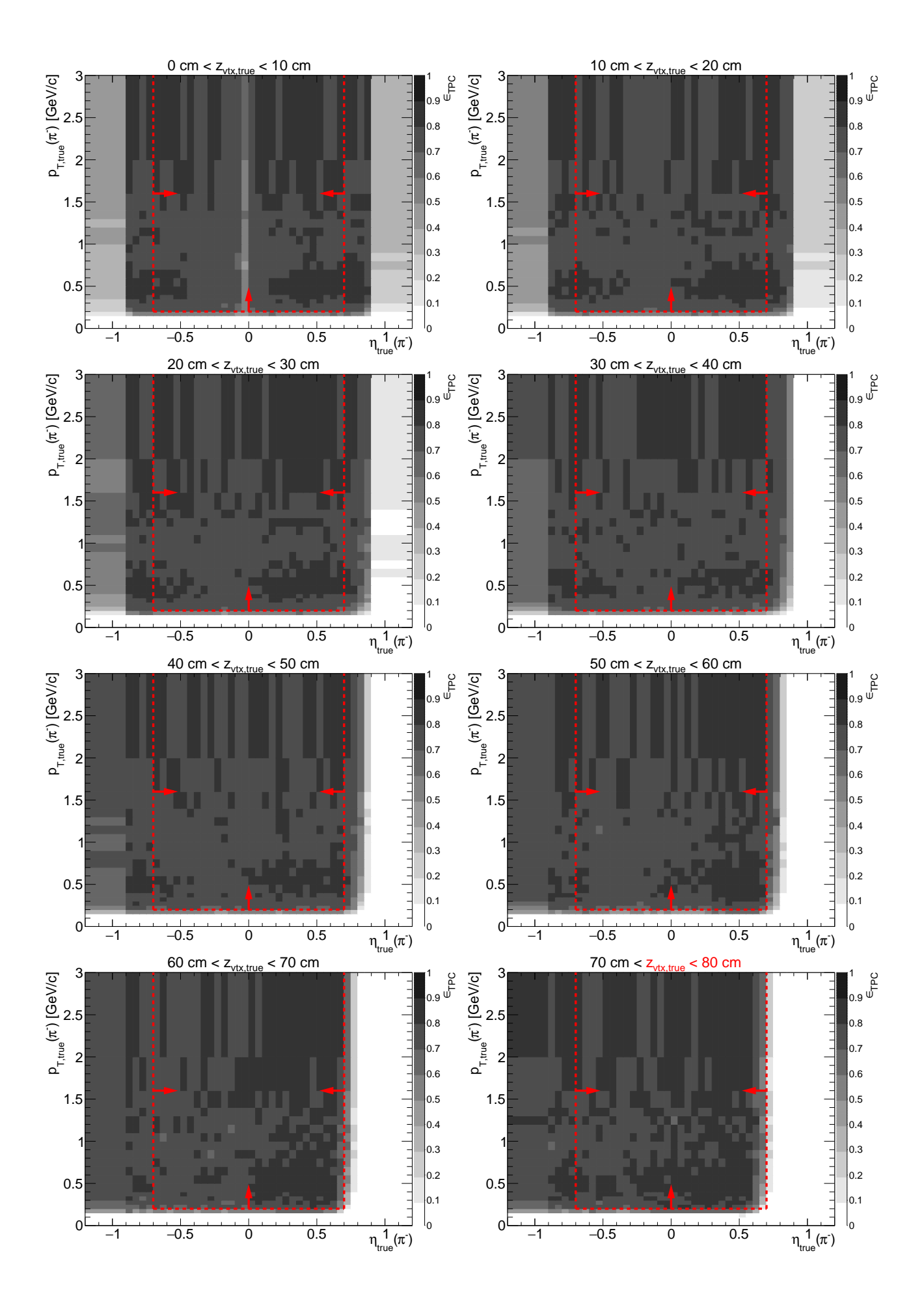
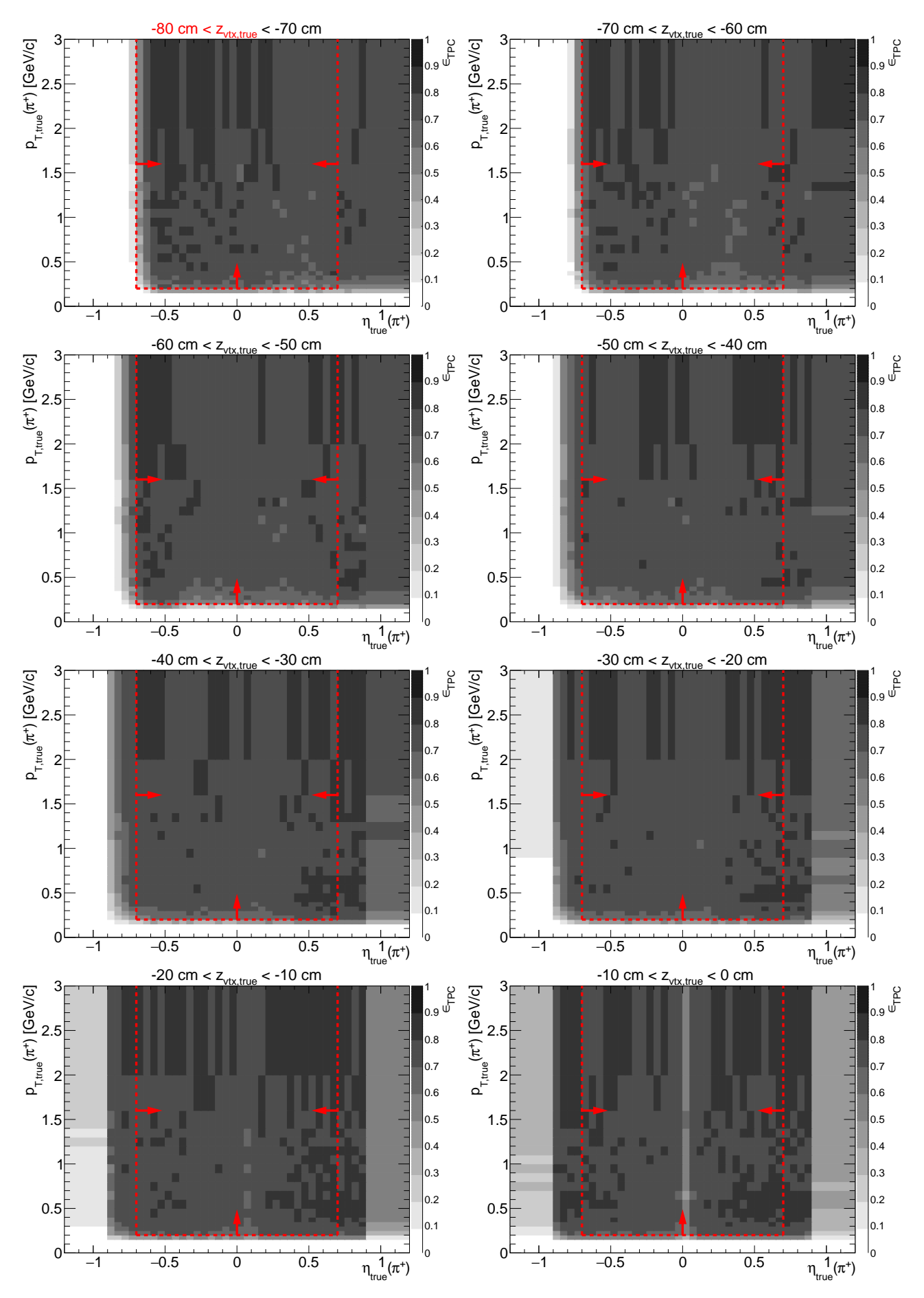


Figure 1.2: TPC acceptance and reconstruction efficiency of  $\pi^+$ . Each plot represents the TPC efficiency  $\epsilon_{\text{TPC}}$  (z-axis) as a function of true particle pseudorapidity  $\eta$  (x-axis) and transverse momentum  $p_T$  (y-axis) in single z-vertex bin whose range is given at the top. Red lines and arrows indicate region accepted in analyses.



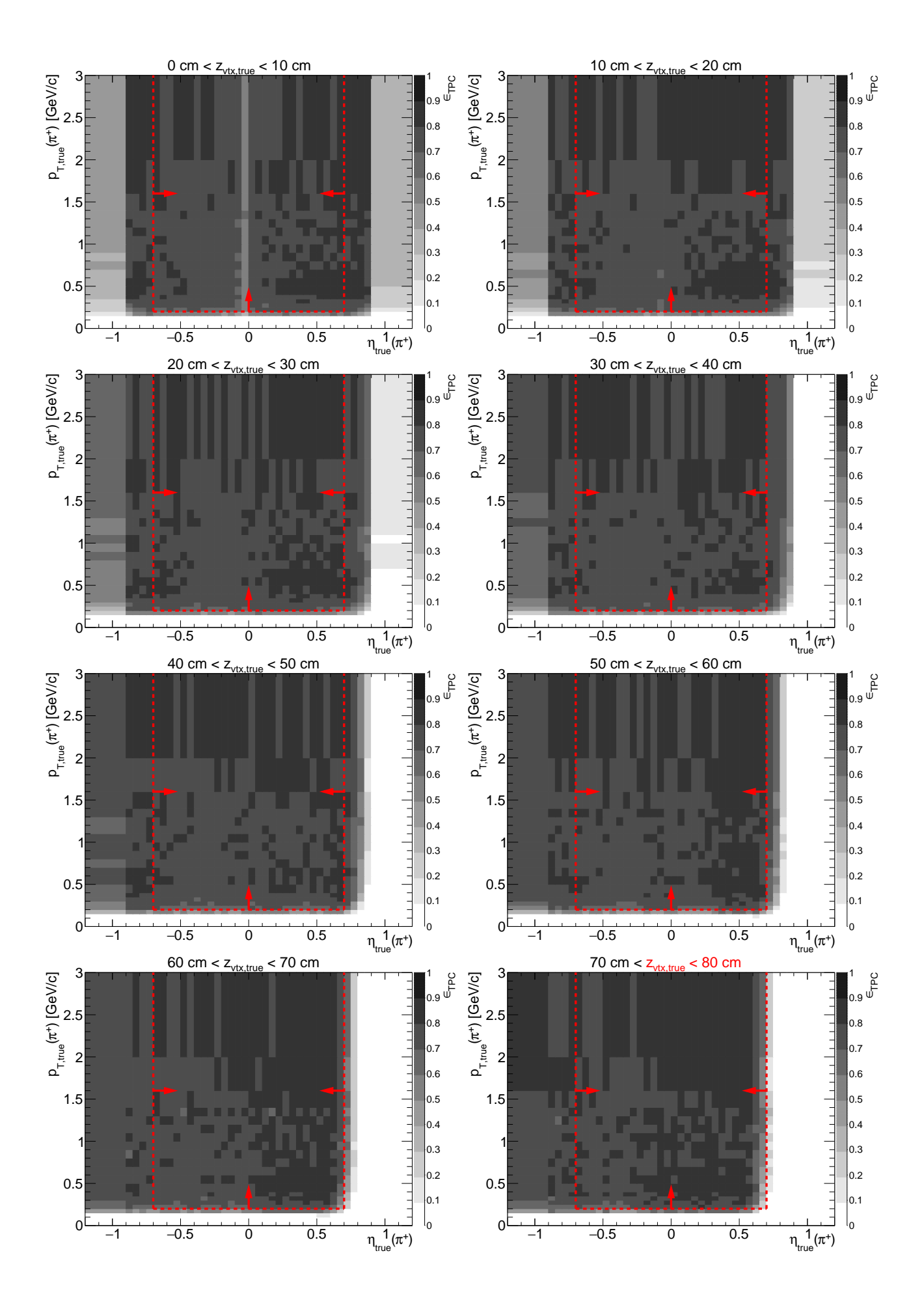
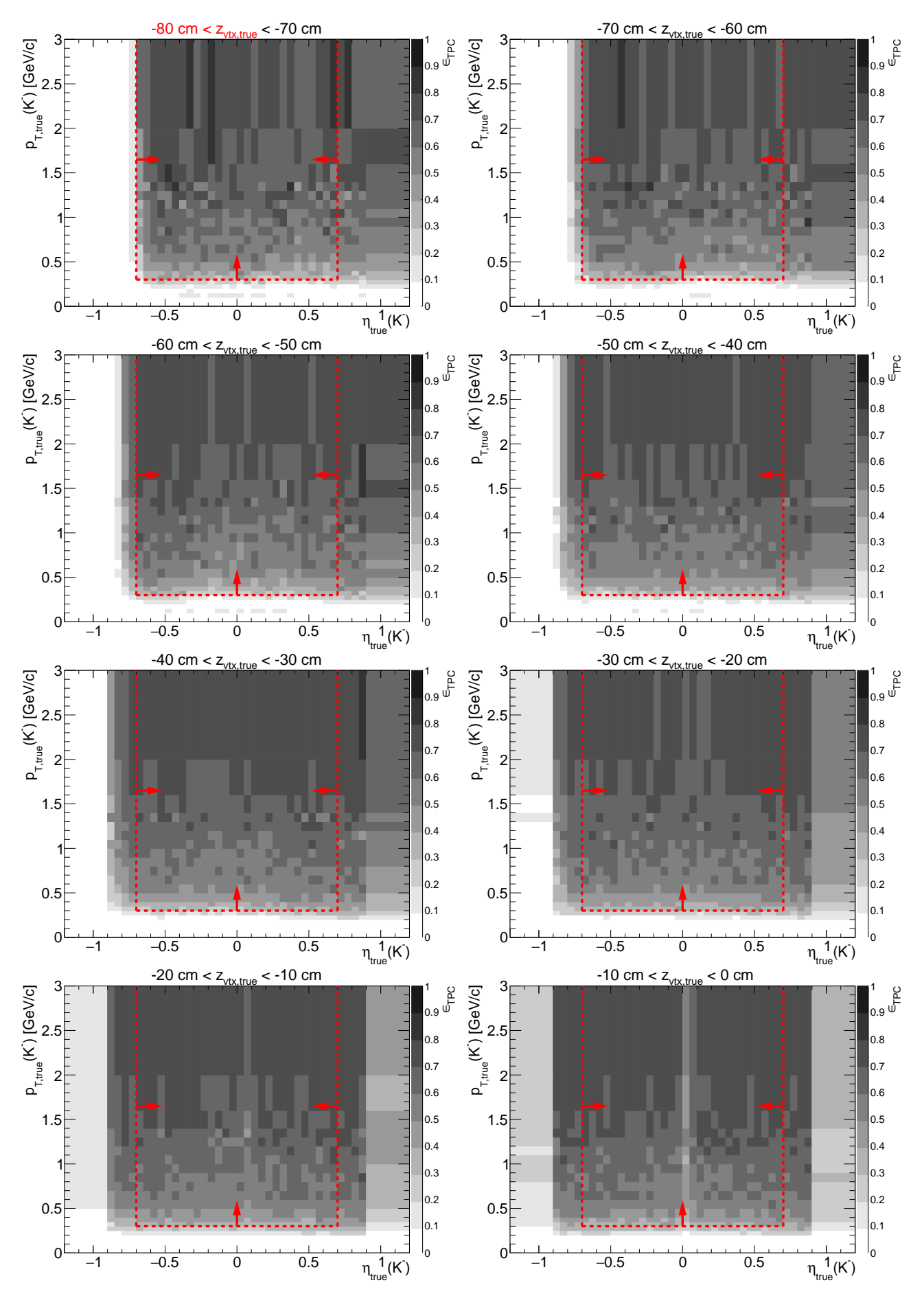


Figure 1.3: TPC acceptance and reconstruction efficiency of  $K^-$ . Each plot represents the TPC efficiency  $\epsilon_{\text{TPC}}$  (z-axis) as a function of true particle pseudorapidity  $\eta$  (x-axis) and transverse momentum  $p_T$  (y-axis) in single z-vertex bin whose range is given at the top. Red lines and arrows indicate region accepted in analyses.



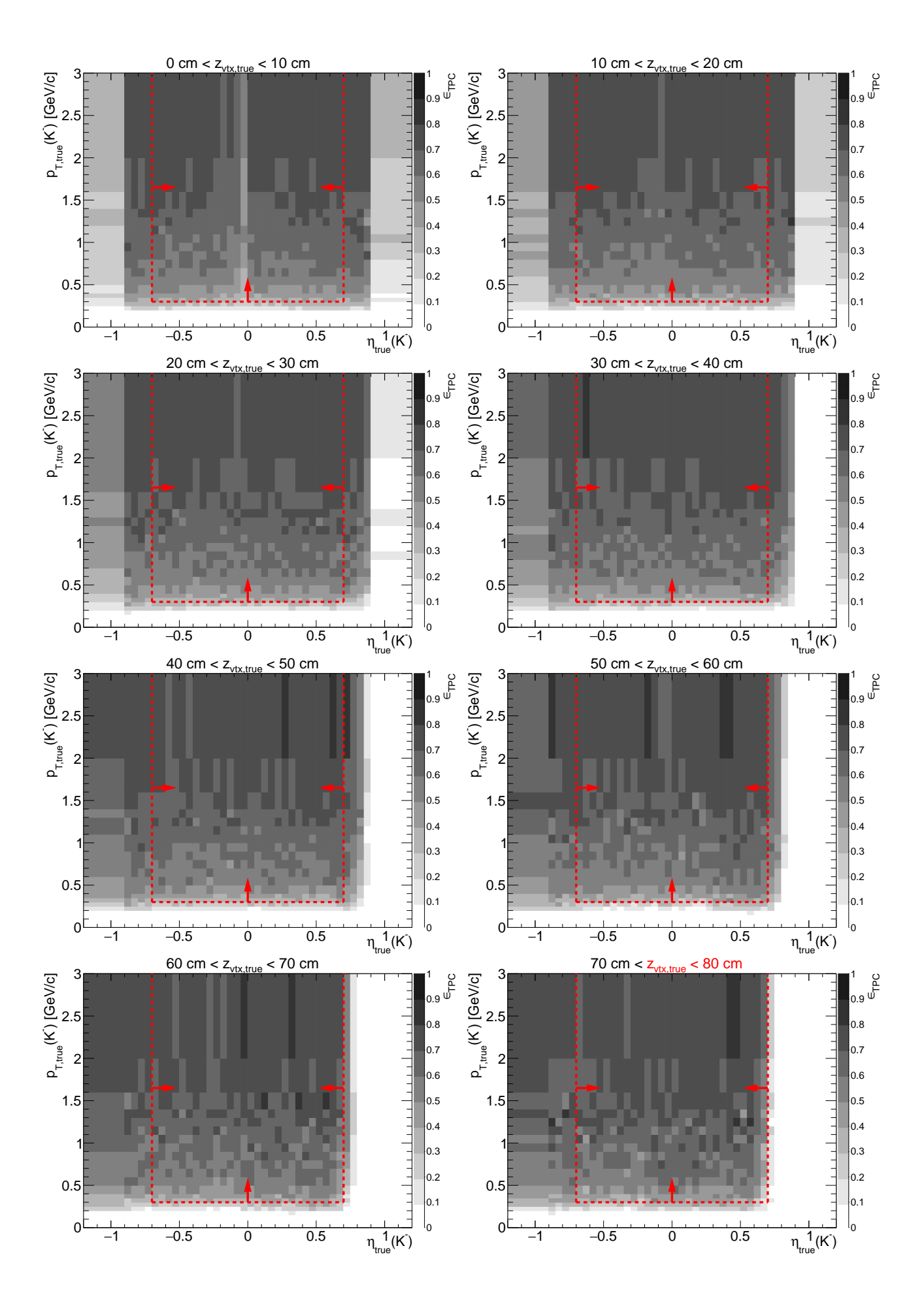
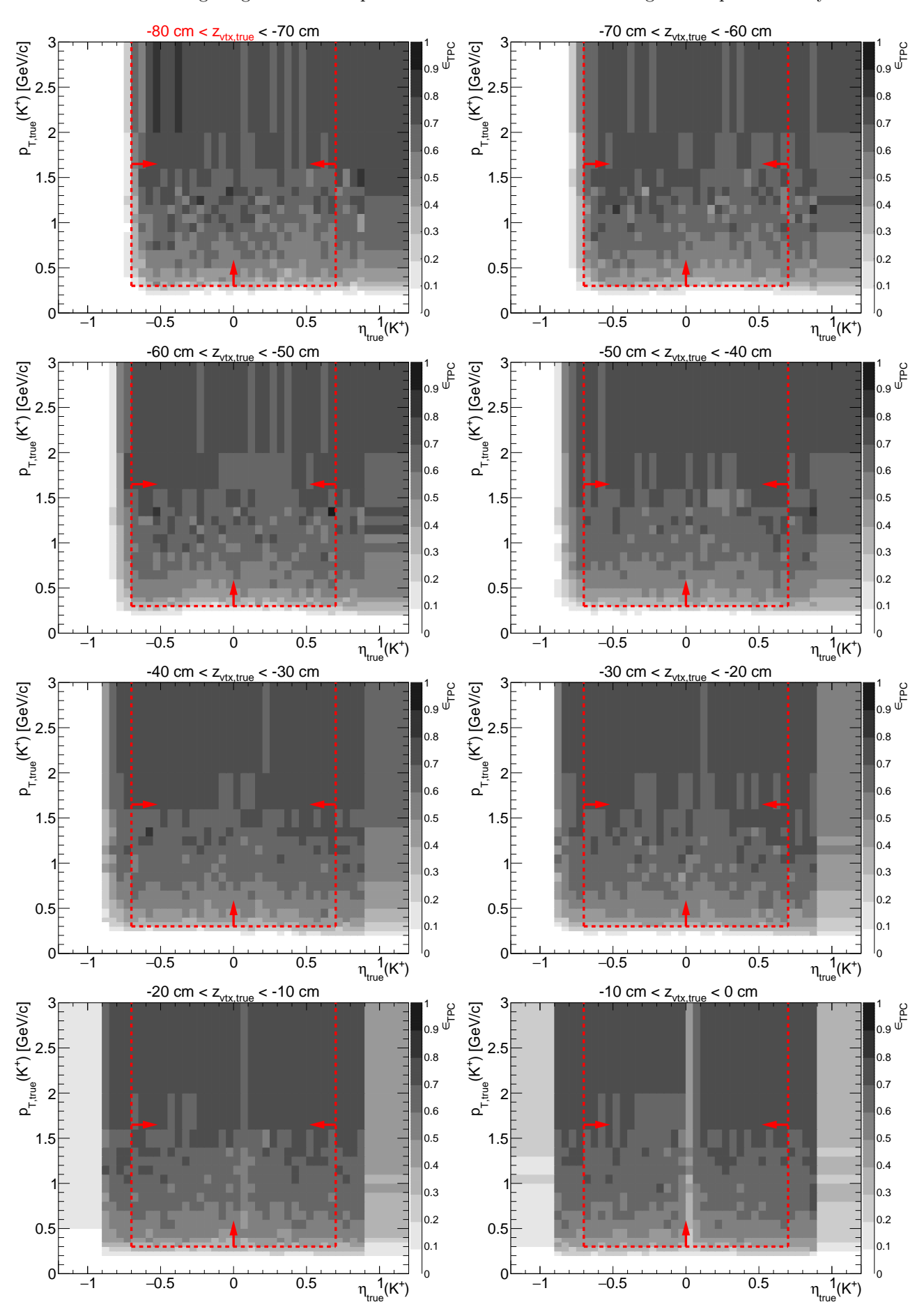


Figure 1.4: TPC acceptance and reconstruction efficiency of  $K^+$ . Each plot represents the TPC efficiency  $\epsilon_{\text{TPC}}$  (z-axis) as a function of true particle pseudorapidity  $\eta$  (x-axis) and transverse momentum  $p_T$  (y-axis) in single z-vertex bin whose range is given at the top. Red lines and arrows indicate region accepted in analyses.



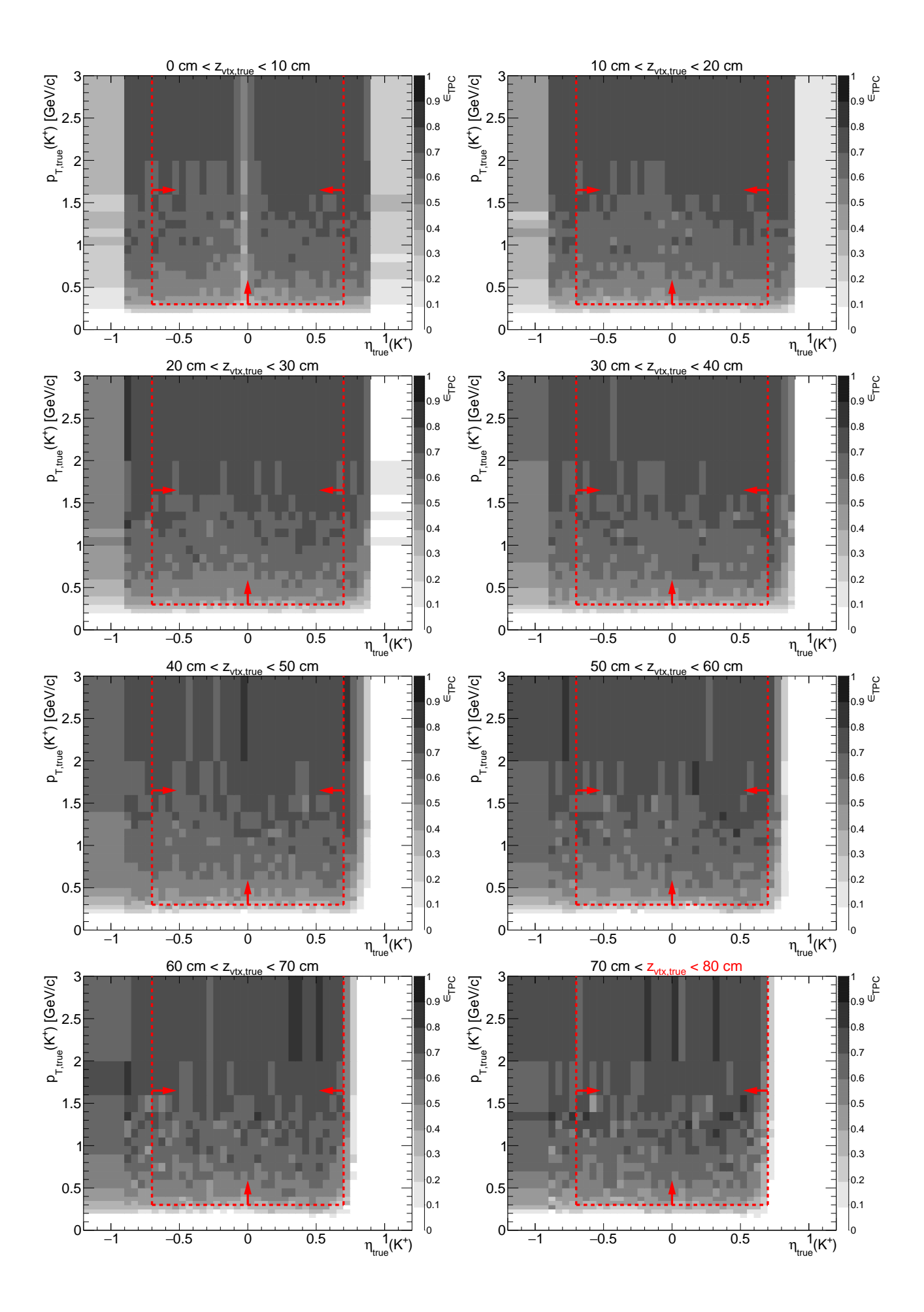
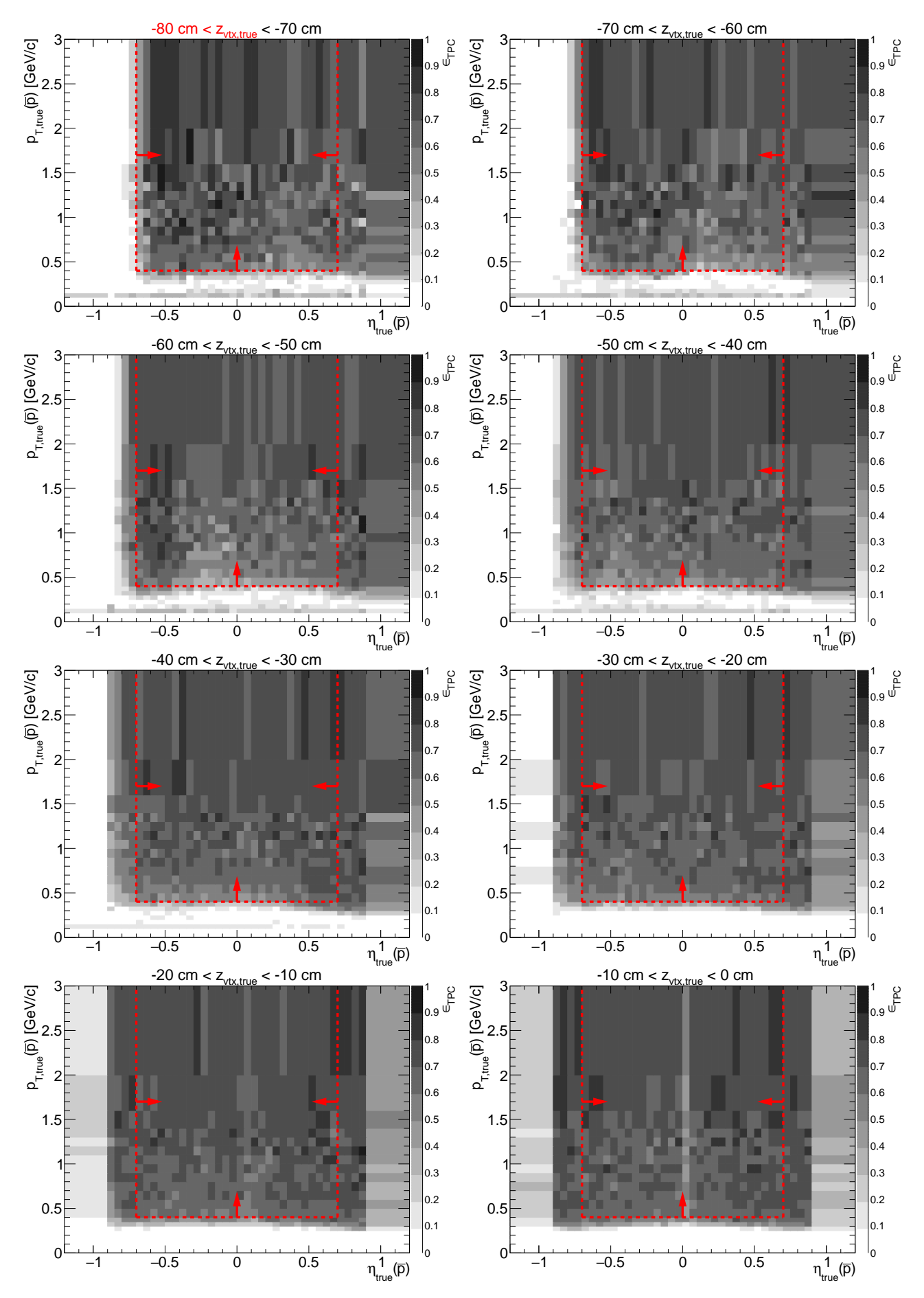


Figure 1.5: TPC acceptance and reconstruction efficiency of  $\bar{p}$ . Each plot represents the TPC efficiency  $\epsilon_{\text{TPC}}$  (z-axis) as a function of true particle pseudorapidity  $\eta$  (x-axis) and transverse momentum  $p_T$  (y-axis) in single z-vertex bin whose range is given at the top. Red lines and arrows indicate region accepted in analyses.



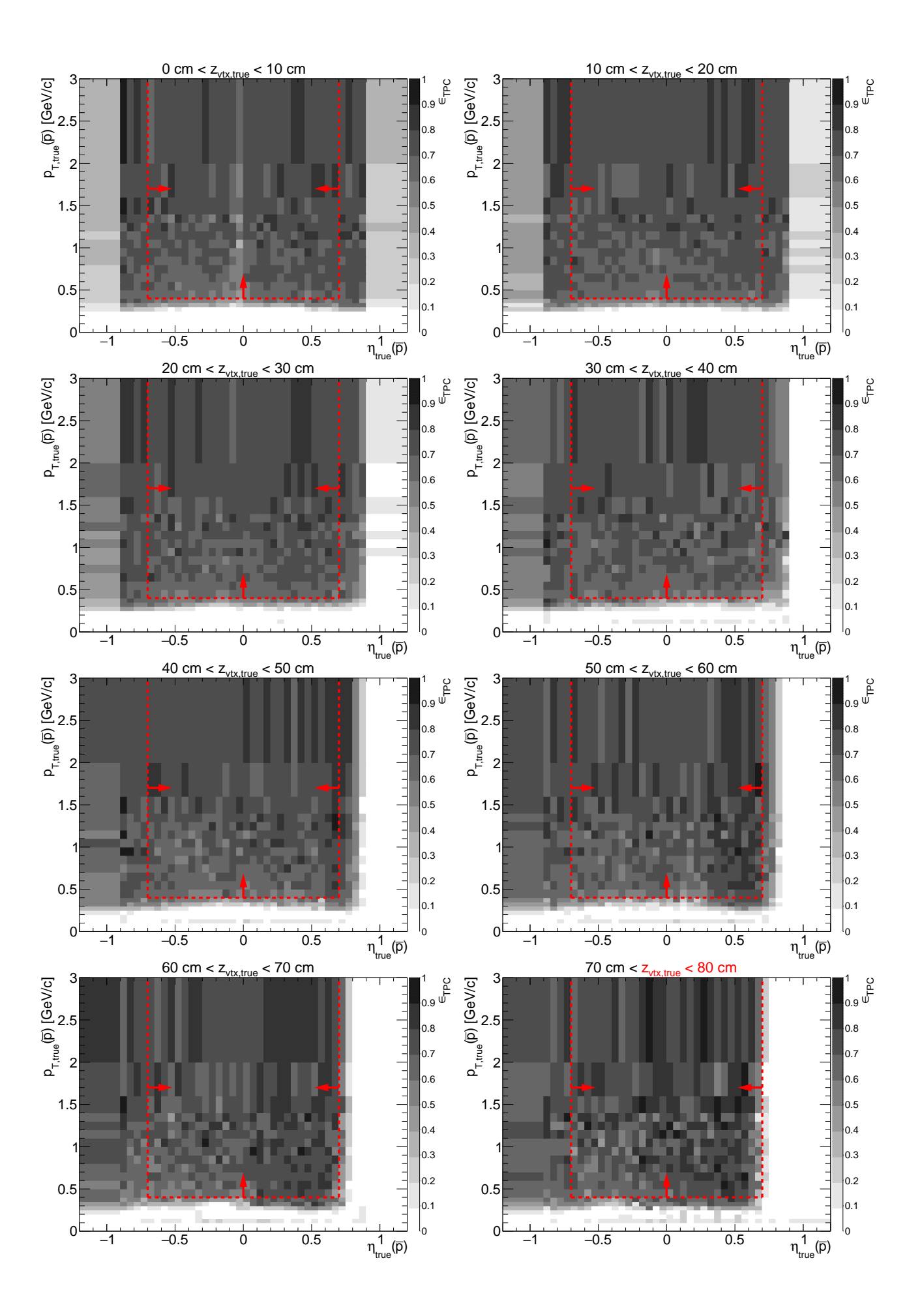
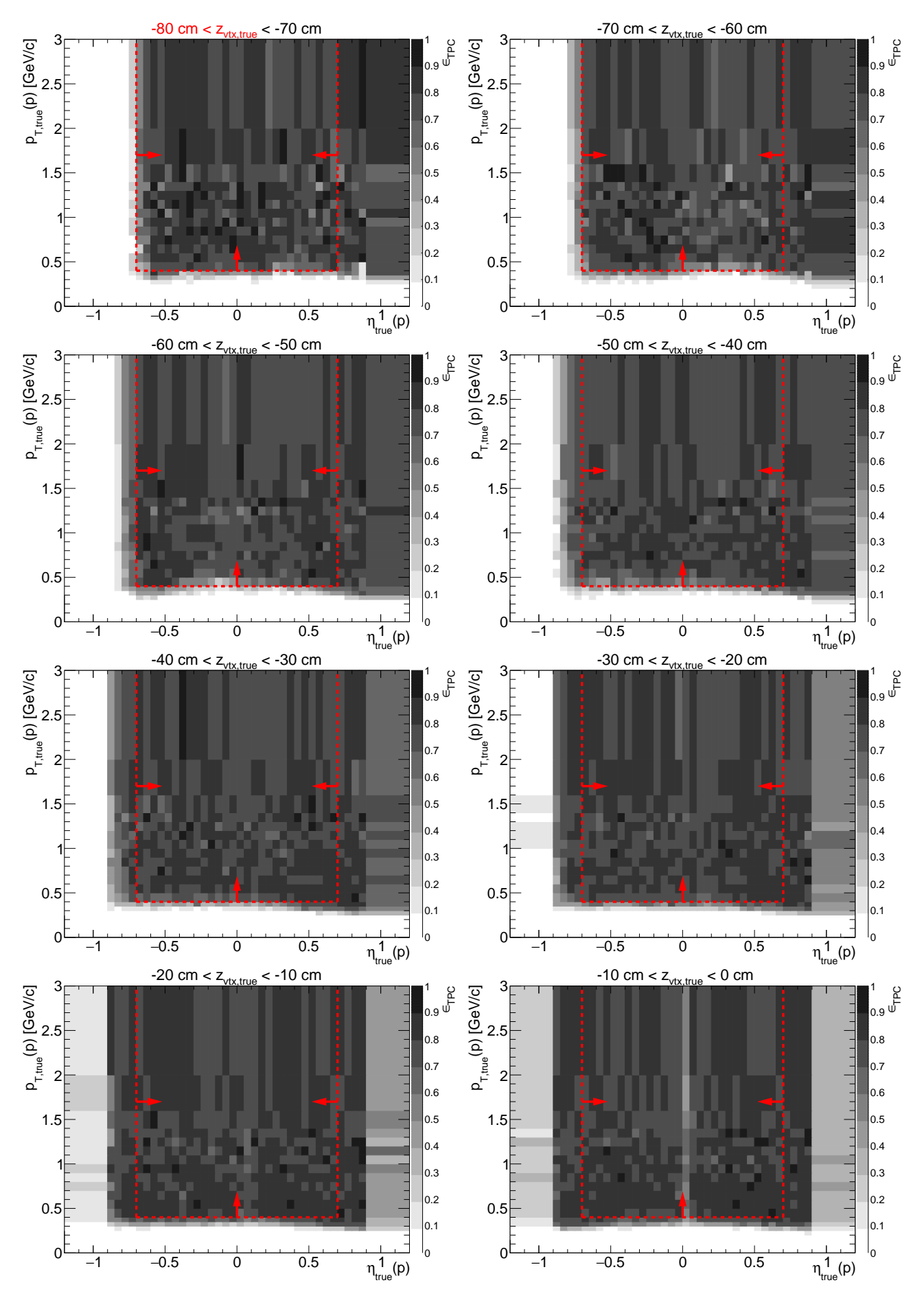
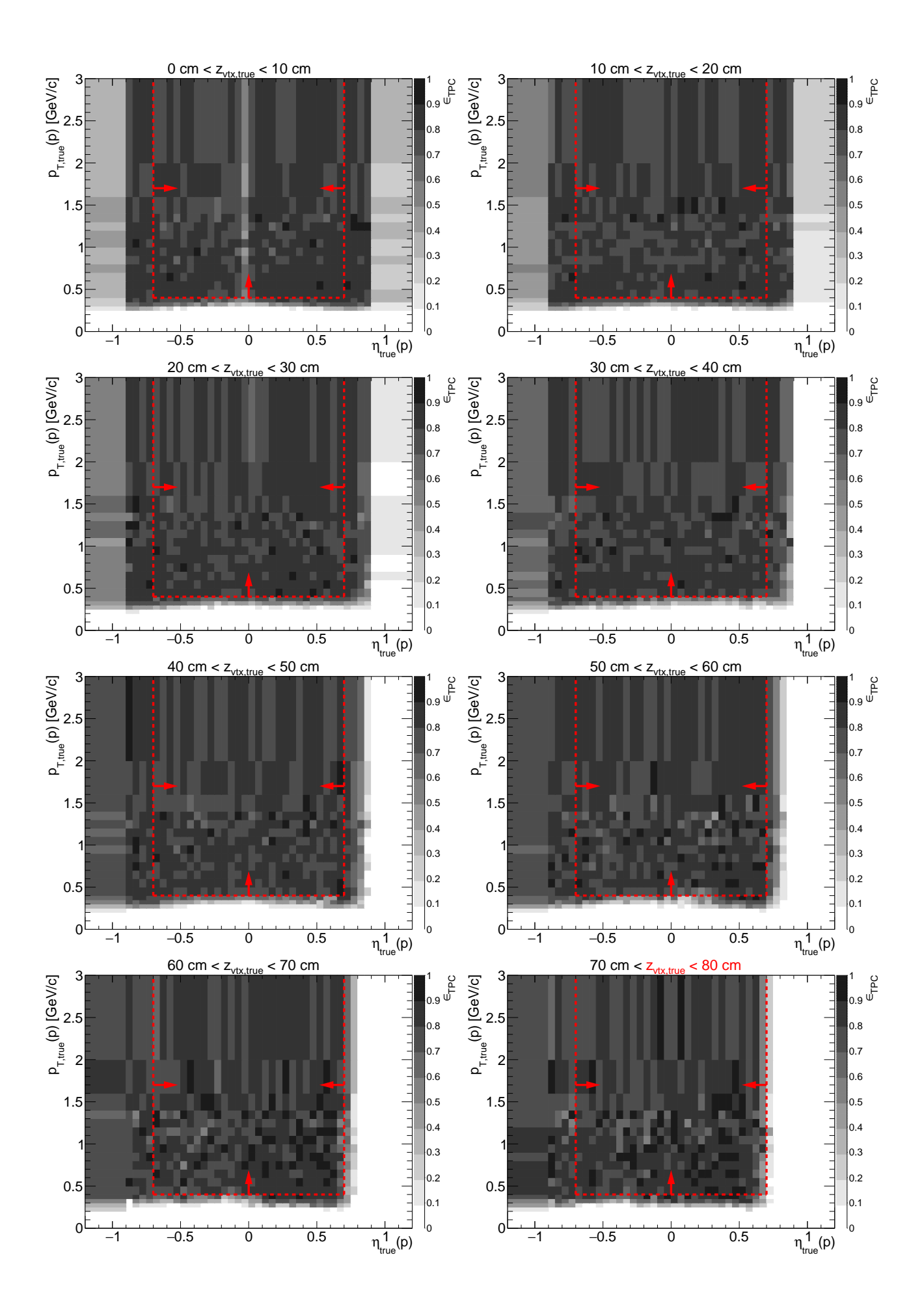


Figure 1.6: TPC acceptance and reconstruction efficiency of p. Each plot represents the TPC efficiency  $\epsilon_{\text{TPC}}$  (z-axis) as a function of true particle pseudorapidity  $\eta$  (x-axis) and transverse momentum  $p_T$  (y-axis) in single z-vertex bin whose range is given at the top. Red lines and arrows indicate region accepted in analyses.





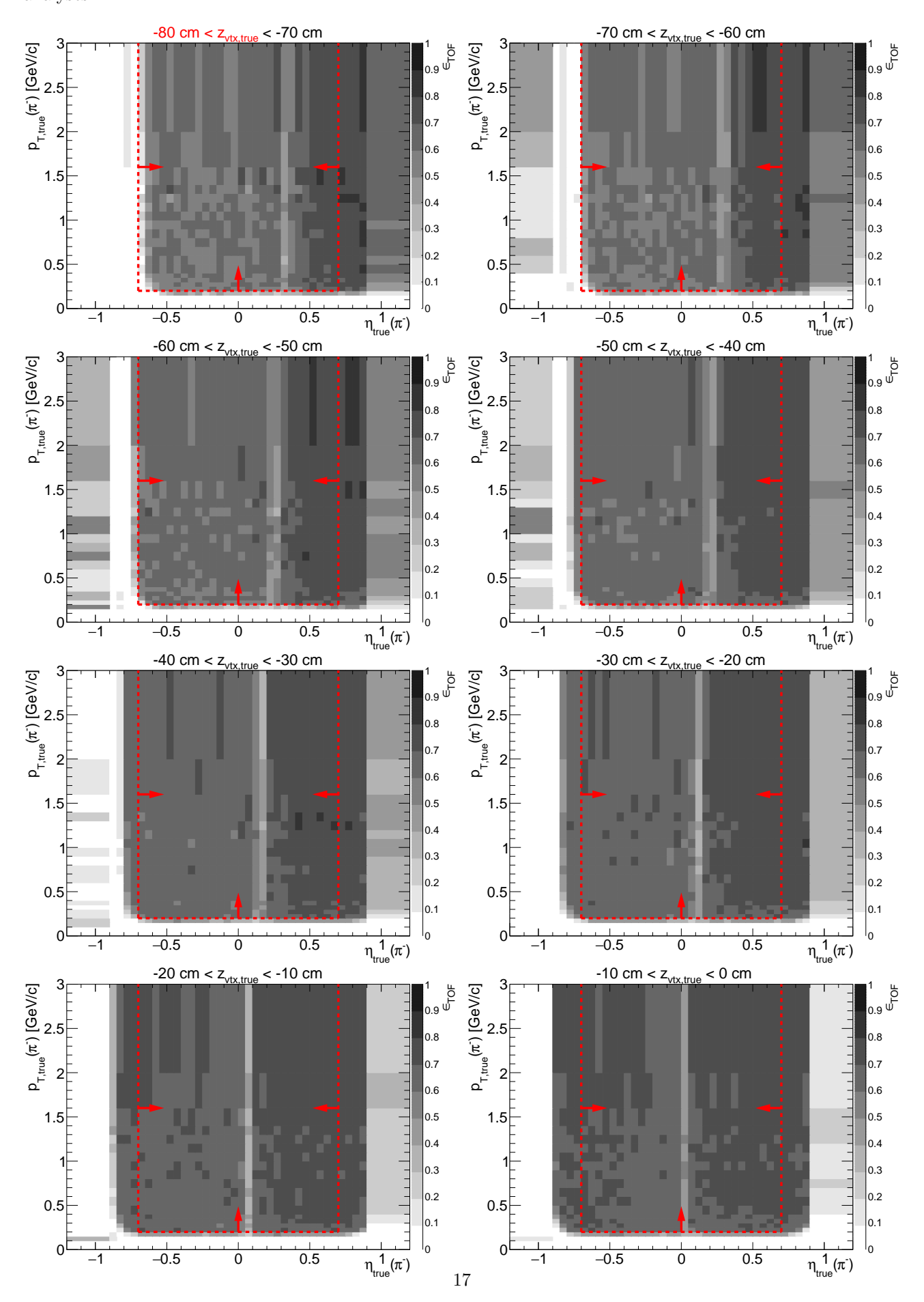
#### 1.2 TOF acceptance, hit reconstruction and track-matching efficiency

Combined TOF acceptance, hit reconstruction efficiency and matching efficiency with TPC tracks,  $\epsilon_{\text{TOF}}$ , is defined as the probability that the global TPC track that satisfy kinematic and quality criteria (cuts ?? and ??) is matched with hit in TOF (matching flag of the track is different from 0). This quantity is generally referred as "TOF efficiency".

It is calculated in two ways. In the first approach the STARsim MC embedded into zero-bias triggers is used. Tracks belonging to  $set\ B$  from Sec. ?? are utilized. From these tracks a sub-sample of tracks with non-zero TOF matching flag is extracted ( $set\ C$ ). The TOF efficiency is calculated as

$$\epsilon_{\text{\tiny TOF}}\left(p_T, \eta, z_{vx}; \text{ sign}, \text{PID}\right) = \frac{(p_T, \eta, z_{vx}) \text{ histogram for particles of given sign and ID from } set \ C}{(p_T, \eta, z_{vx}) \text{ histogram for particles of given sign and ID from } set \ B}. \tag{1.2}$$

Figure 1.7: TOF acceptance, reconstruction and matching efficiency of  $\pi^-$ . Each plot represents the TOF efficiency  $\epsilon_{\text{TOF}}$  (z-axis) as a function of true particle pseudorapidity  $\eta$  (x-axis) and transverse momentum  $p_T$  (y-axis) in single z-vertex bin whose range is given at the top. Red lines and arrows indicate region accepted in analyses.



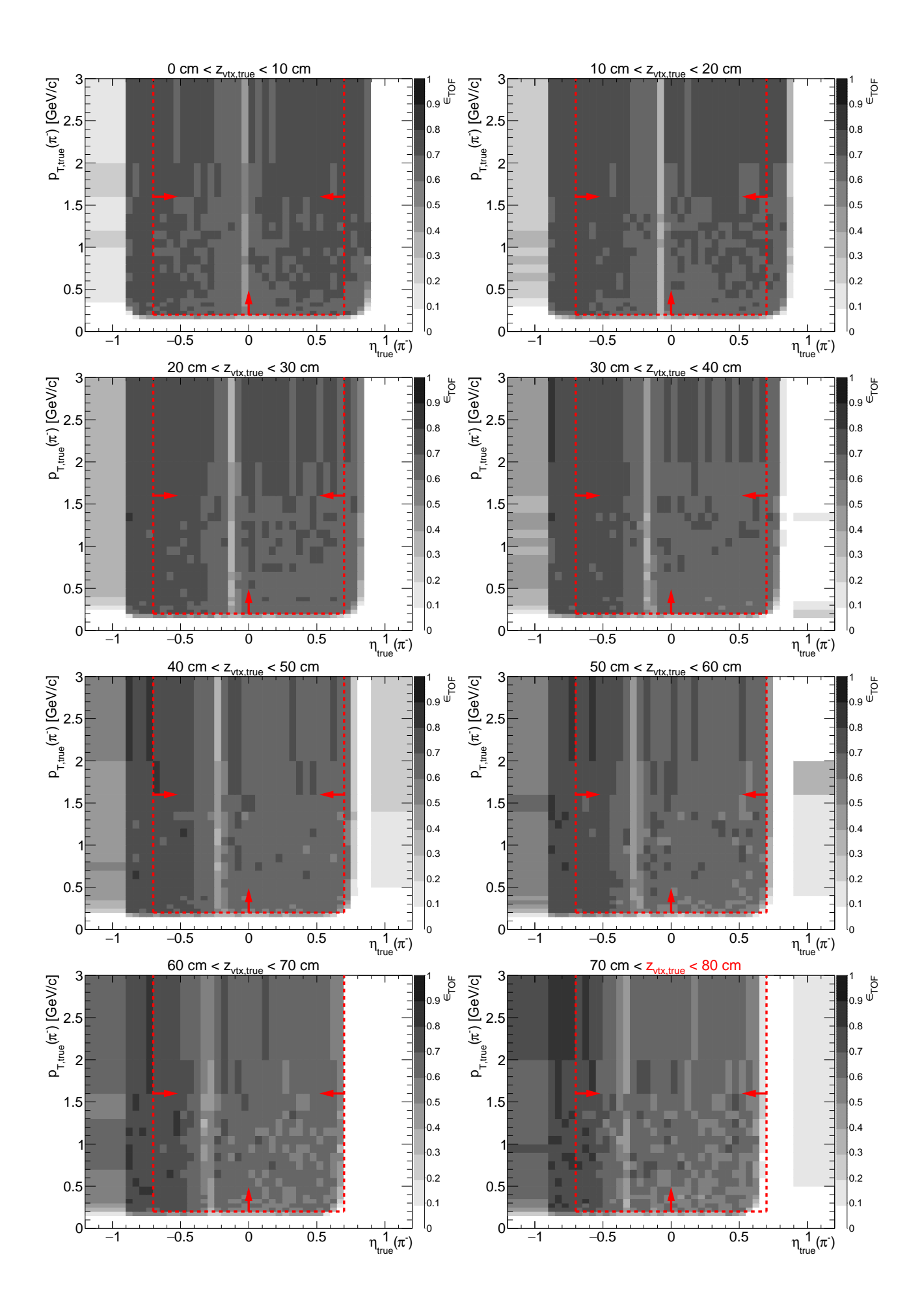
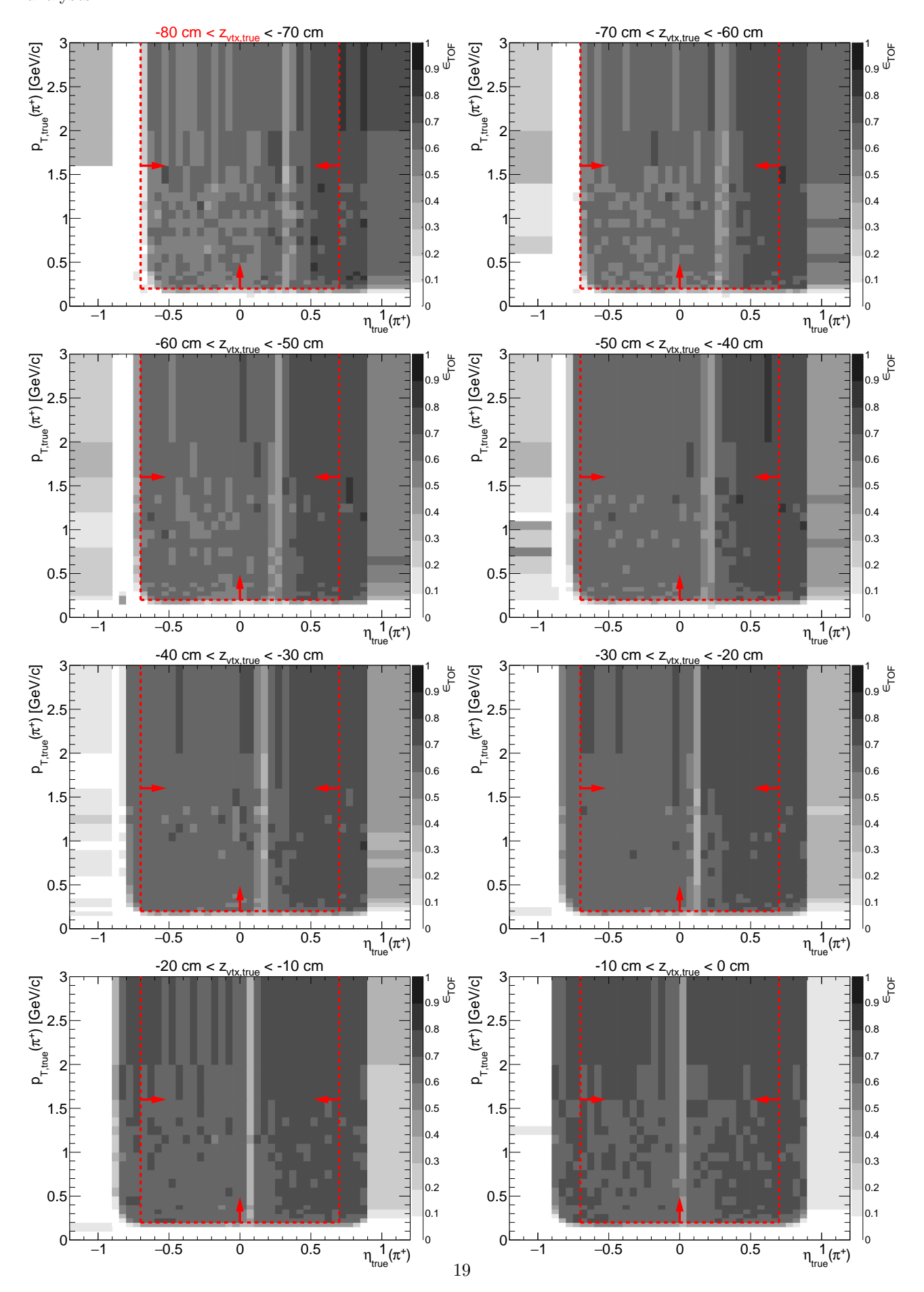


Figure 1.8: TOF acceptance, reconstruction and matching efficiency of  $\pi^+$ . Each plot represents the TOF efficiency  $\epsilon_{\text{TOF}}$  (z-axis) as a function of true particle pseudorapidity  $\eta$  (x-axis) and transverse momentum  $p_T$  (y-axis) in single z-vertex bin whose range is given at the top. Red lines and arrows indicate region accepted in analyses.



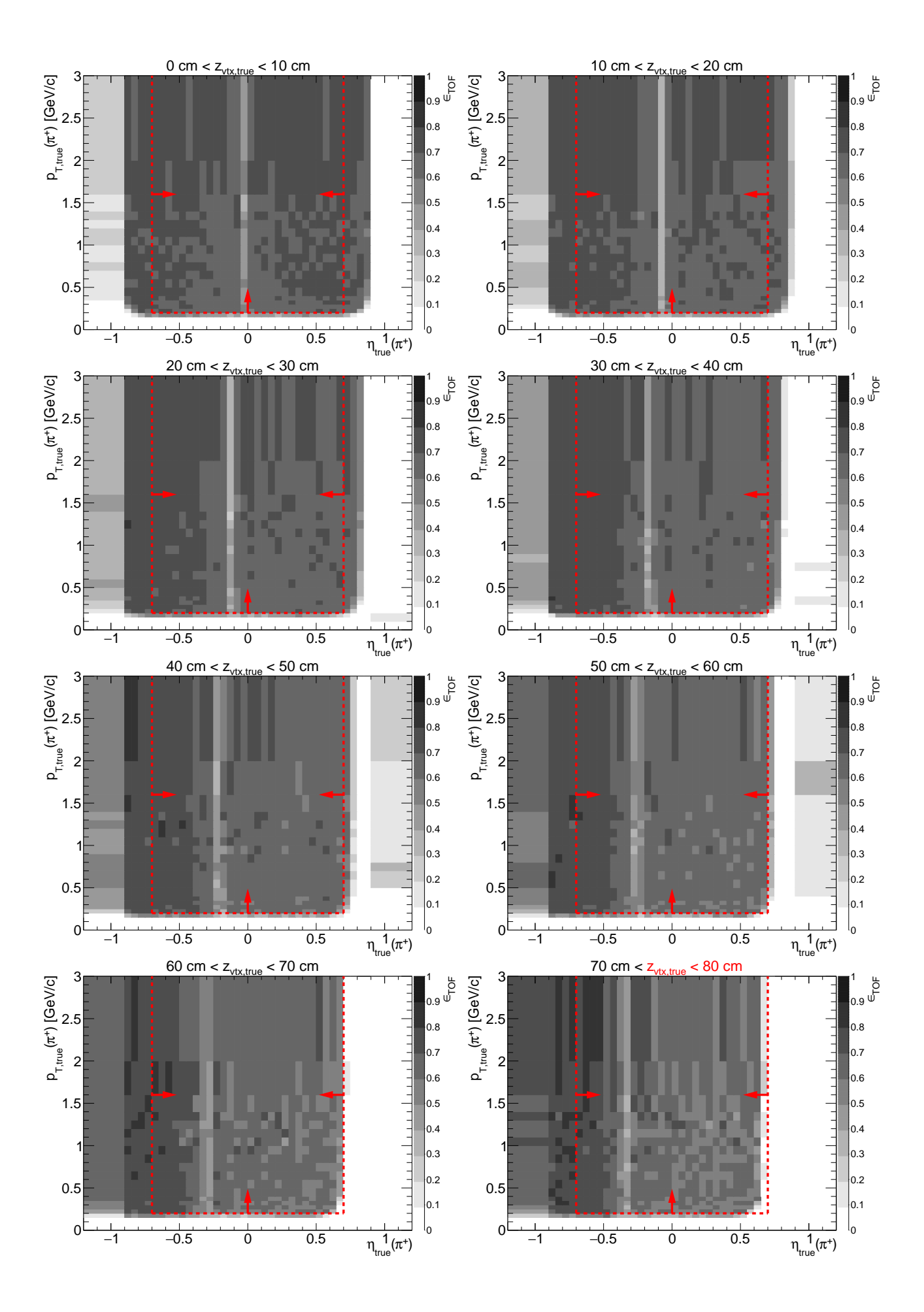
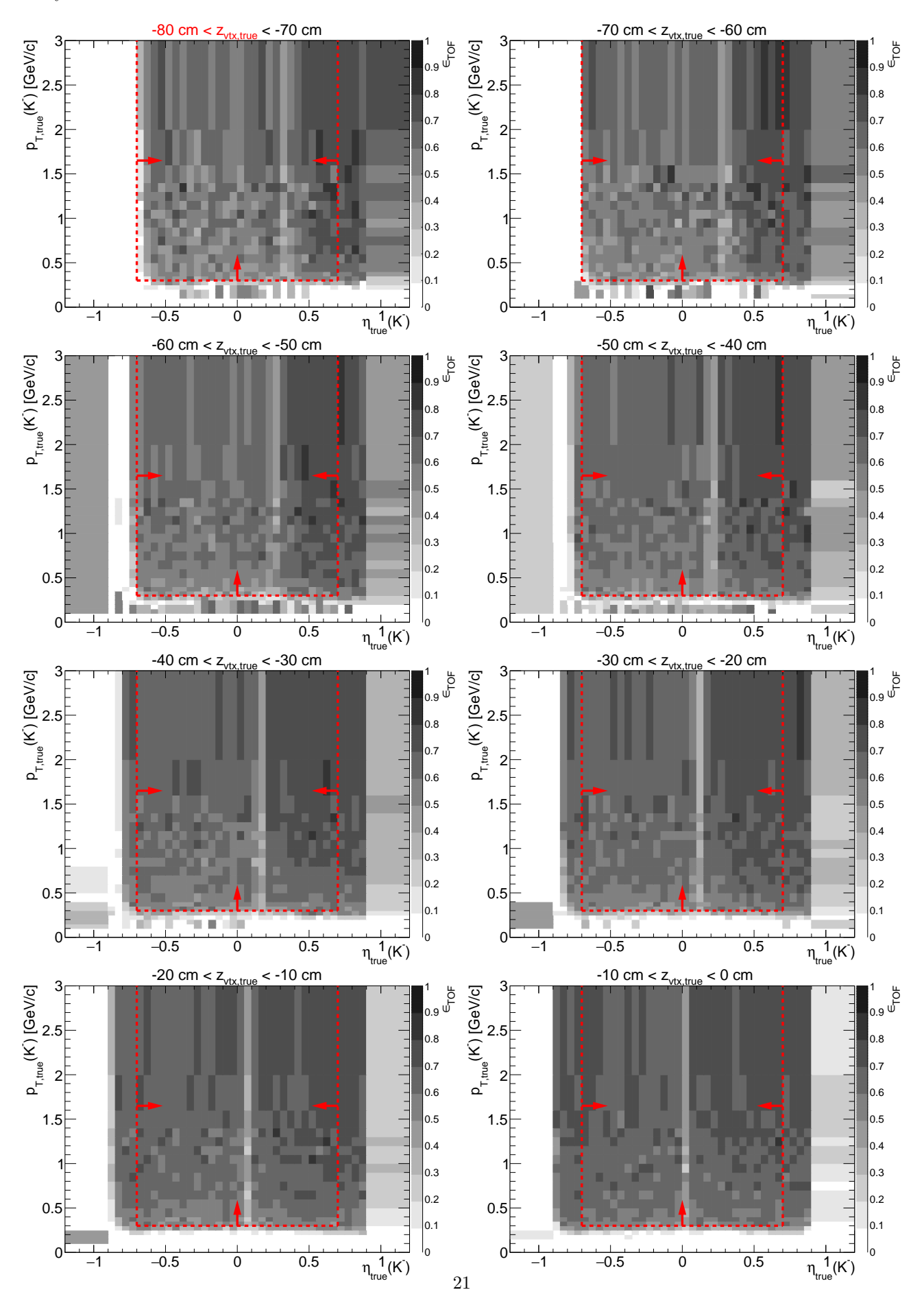


Figure 1.9: TOF acceptance, reconstruction and matching efficiency of  $K^-$ . Each plot represents the TOF efficiency  $\epsilon_{\text{TOF}}$  (z-axis) as a function of true particle pseudorapidity  $\eta$  (x-axis) and transverse momentum  $p_T$  (y-axis) in single z-vertex bin whose range is given at the top. Red lines and arrows indicate region accepted in analyses.



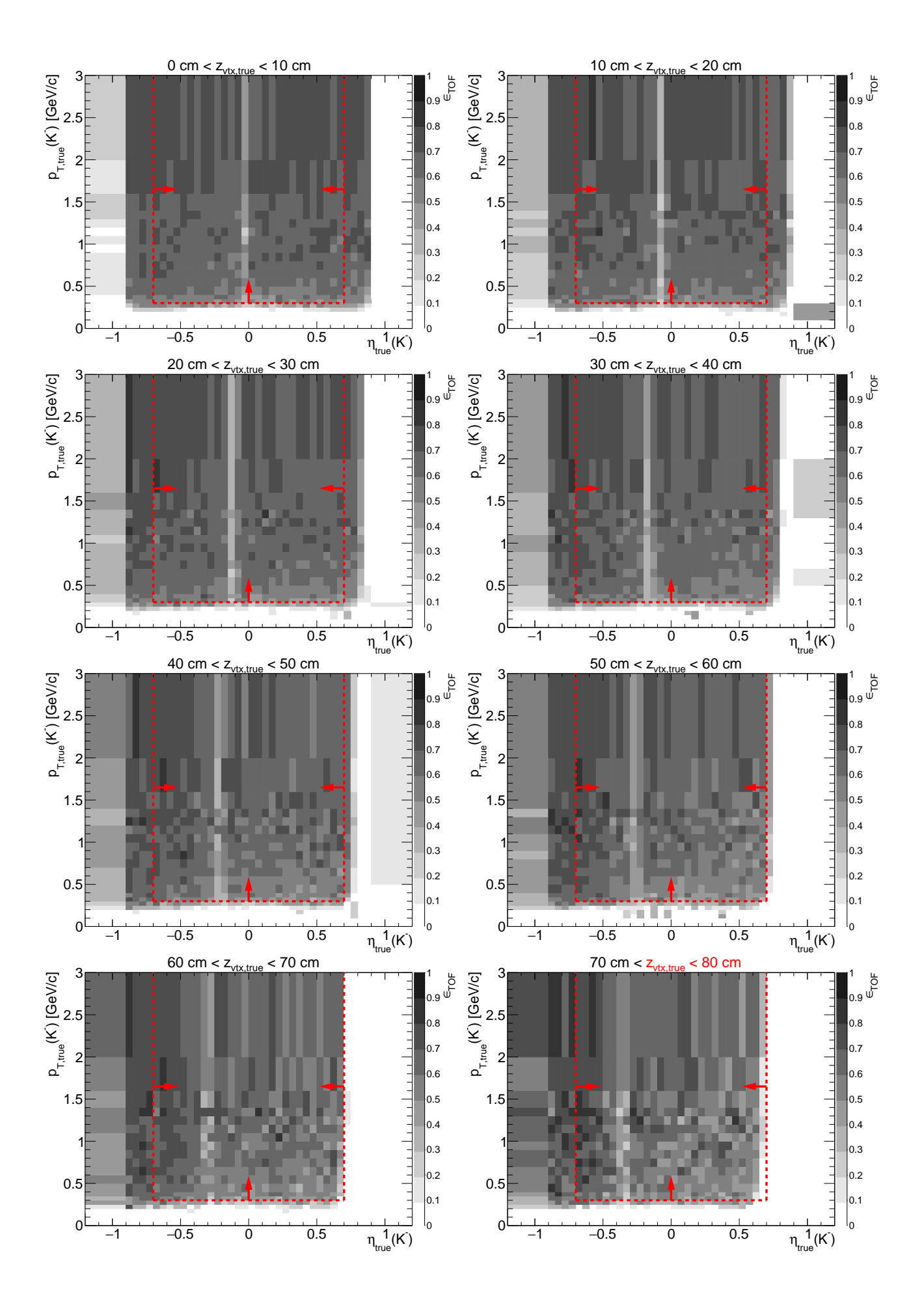
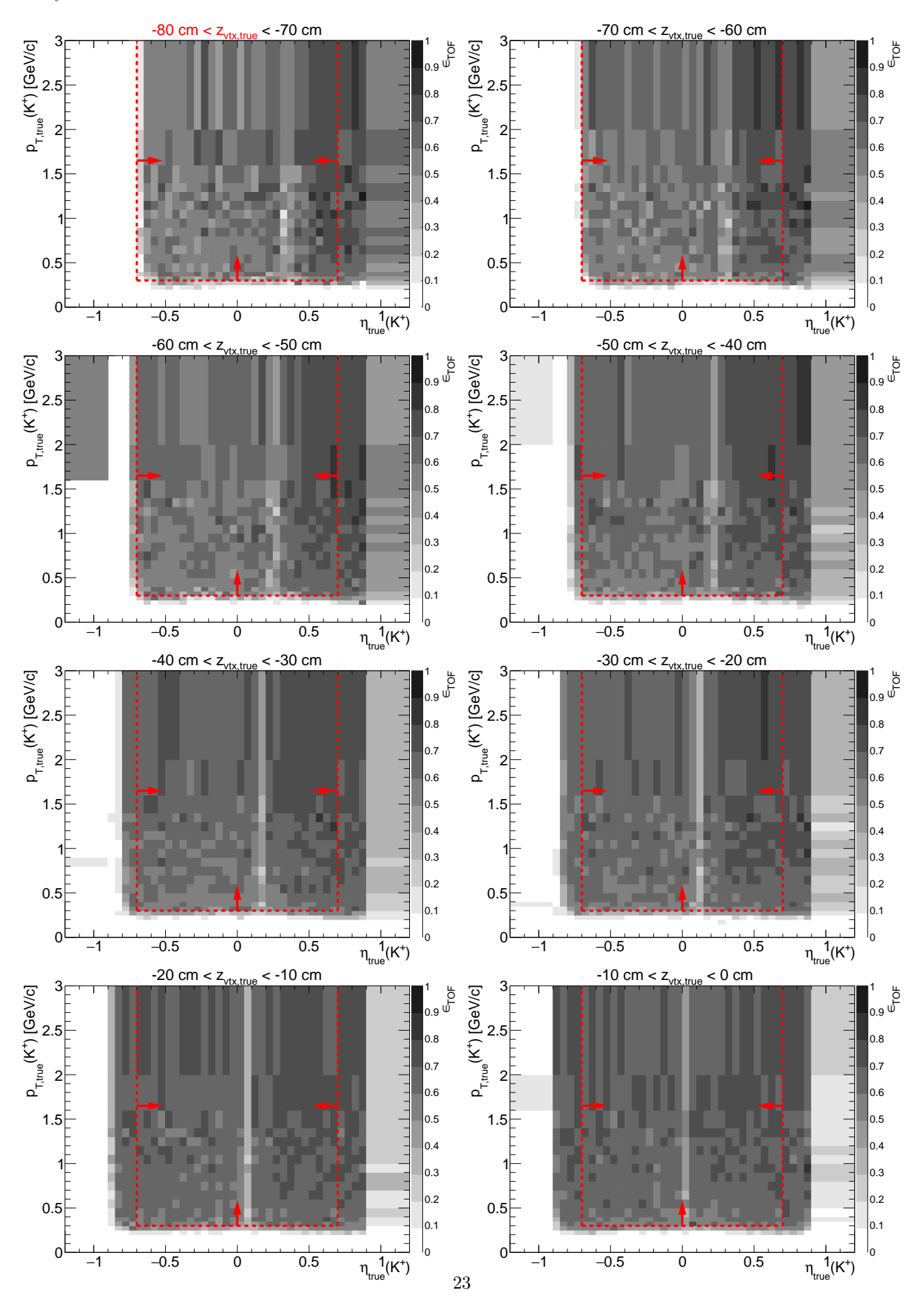


Figure 1.10: TOF acceptance, reconstruction and matching efficiency of  $K^+$ . Each plot represents the TOF efficiency  $\epsilon_{\text{TOF}}$  (z-axis) as a function of true particle pseudorapidity  $\eta$  (x-axis) and transverse momentum  $p_T$  (y-axis) in single z-vertex bin whose range is given at the top. Red lines and arrows indicate region accepted in analyses.



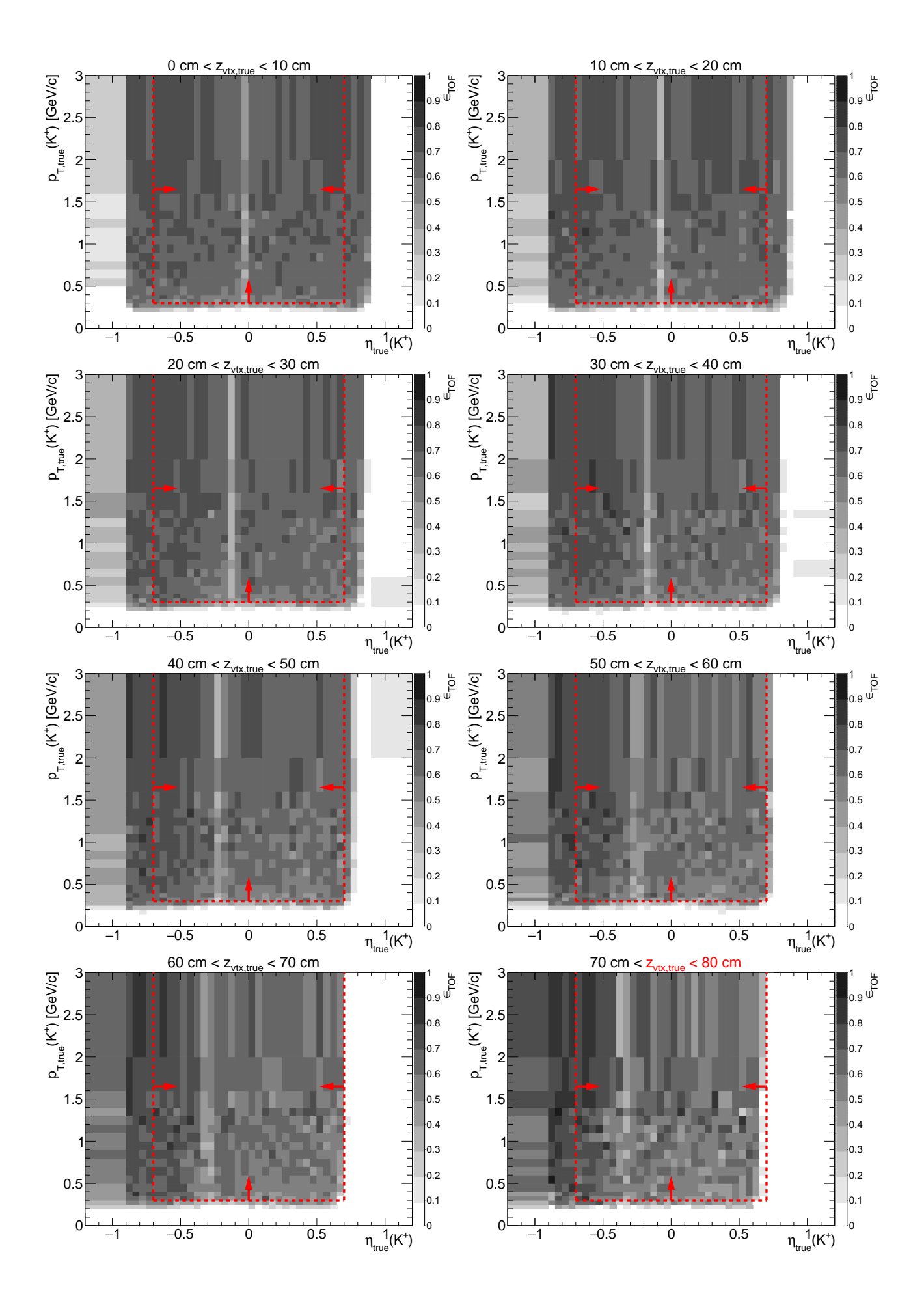
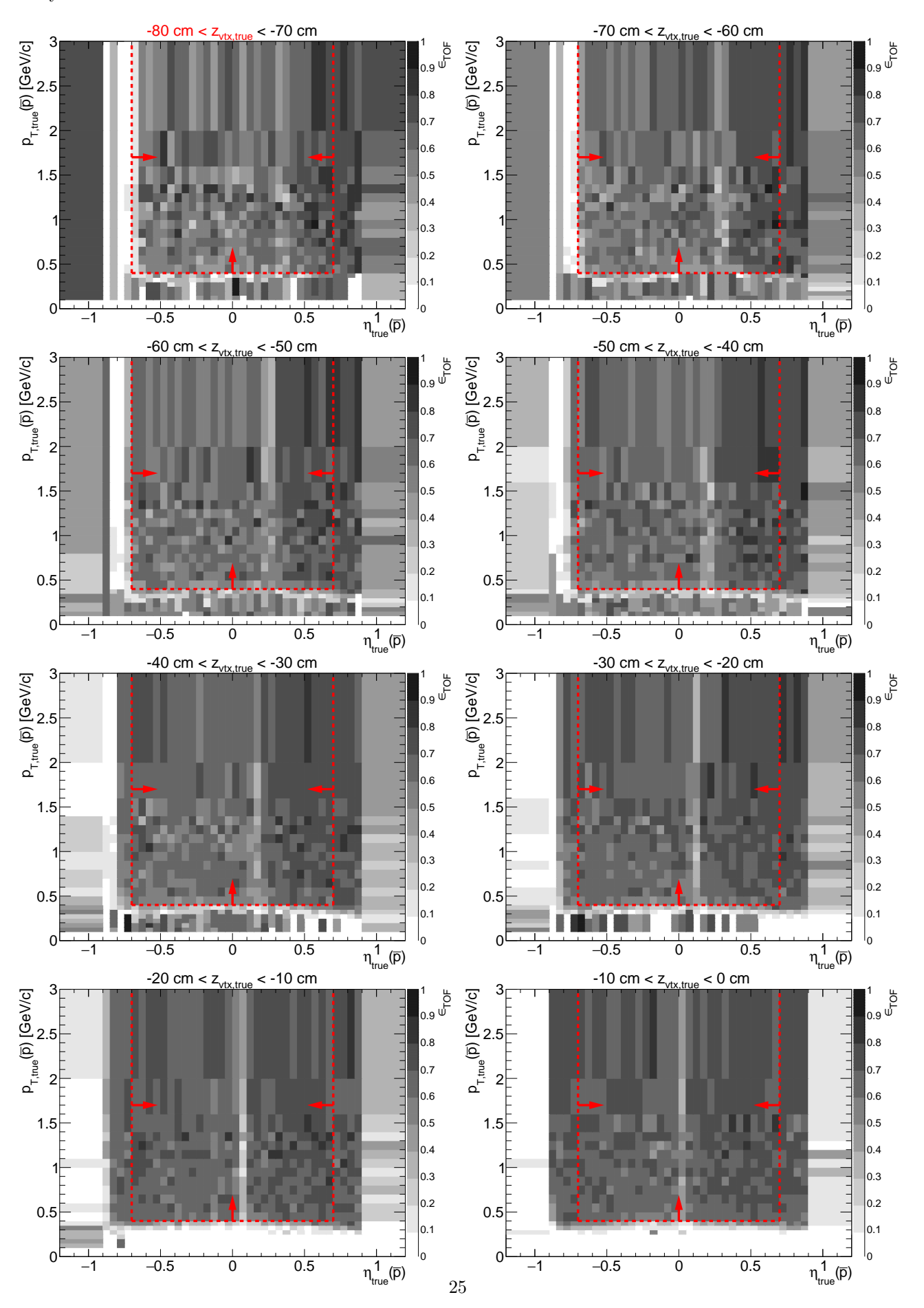


Figure 1.11: TOF acceptance, reconstruction and matching efficiency of  $\bar{p}$ . Each plot represents the TOF efficiency  $\epsilon_{\text{TOF}}$  (z-axis) as a function of true particle pseudorapidity  $\eta$  (x-axis) and transverse momentum  $p_T$  (y-axis) in single z-vertex bin whose range is given at the top. Red lines and arrows indicate region accepted in analyses.



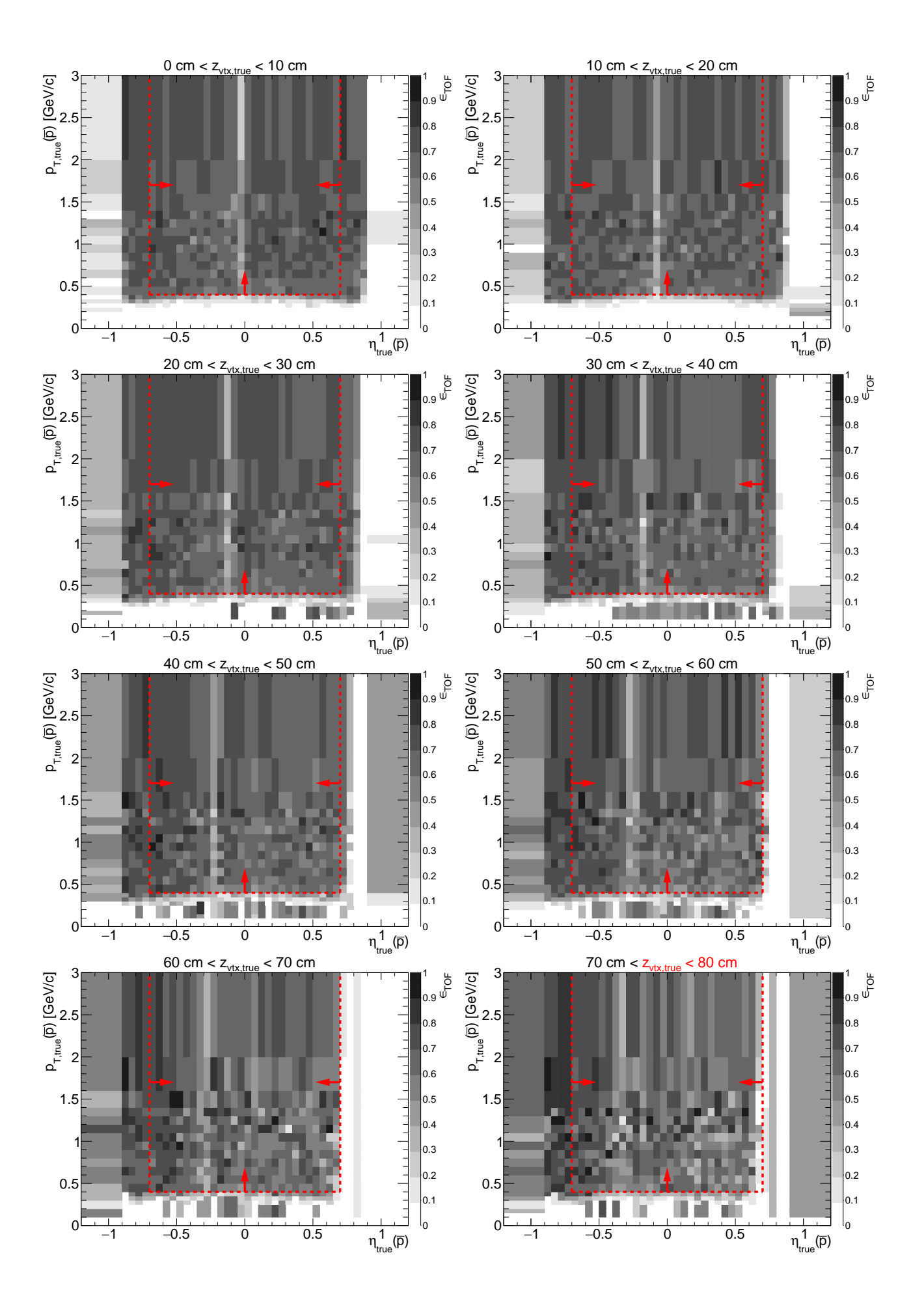
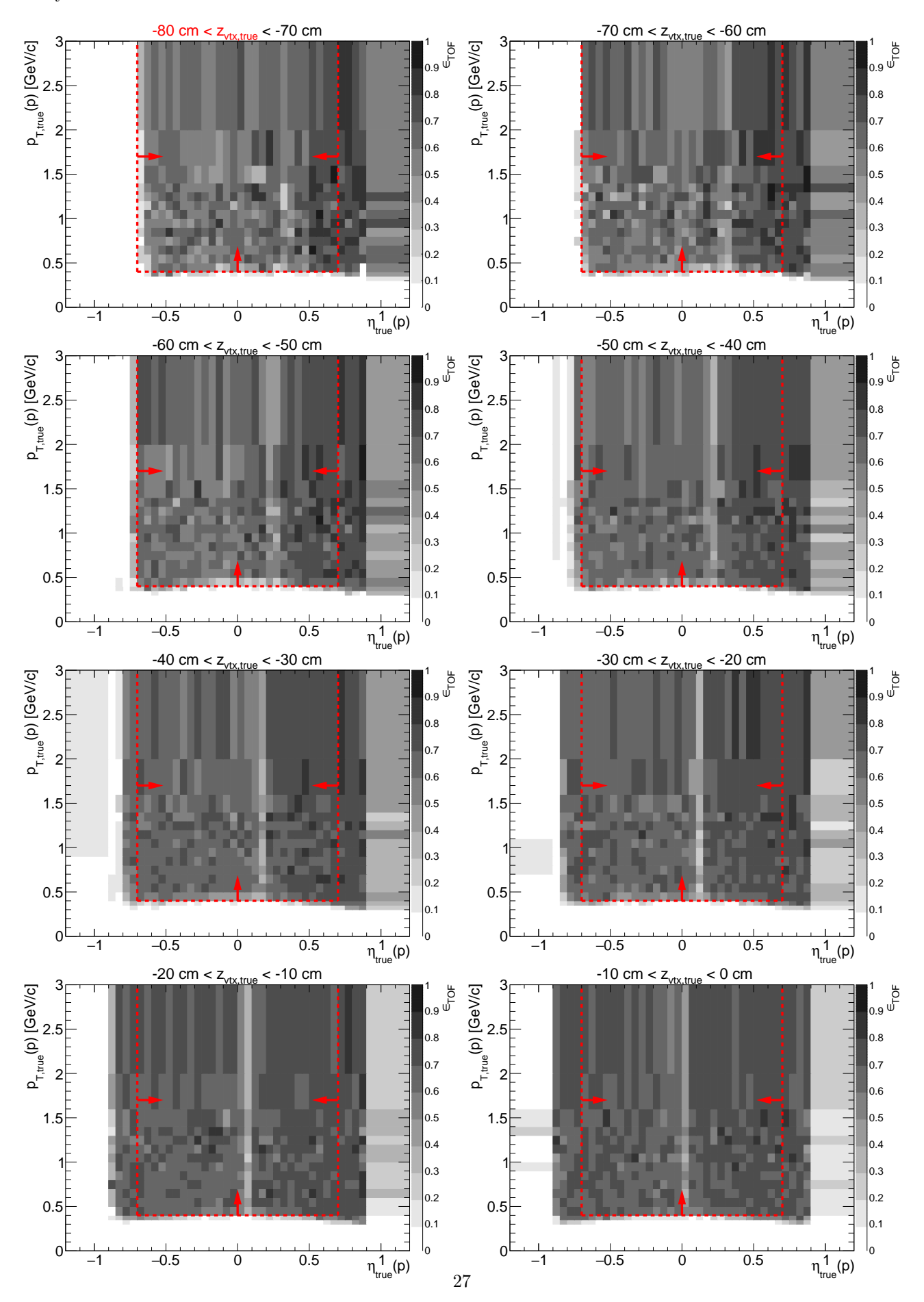
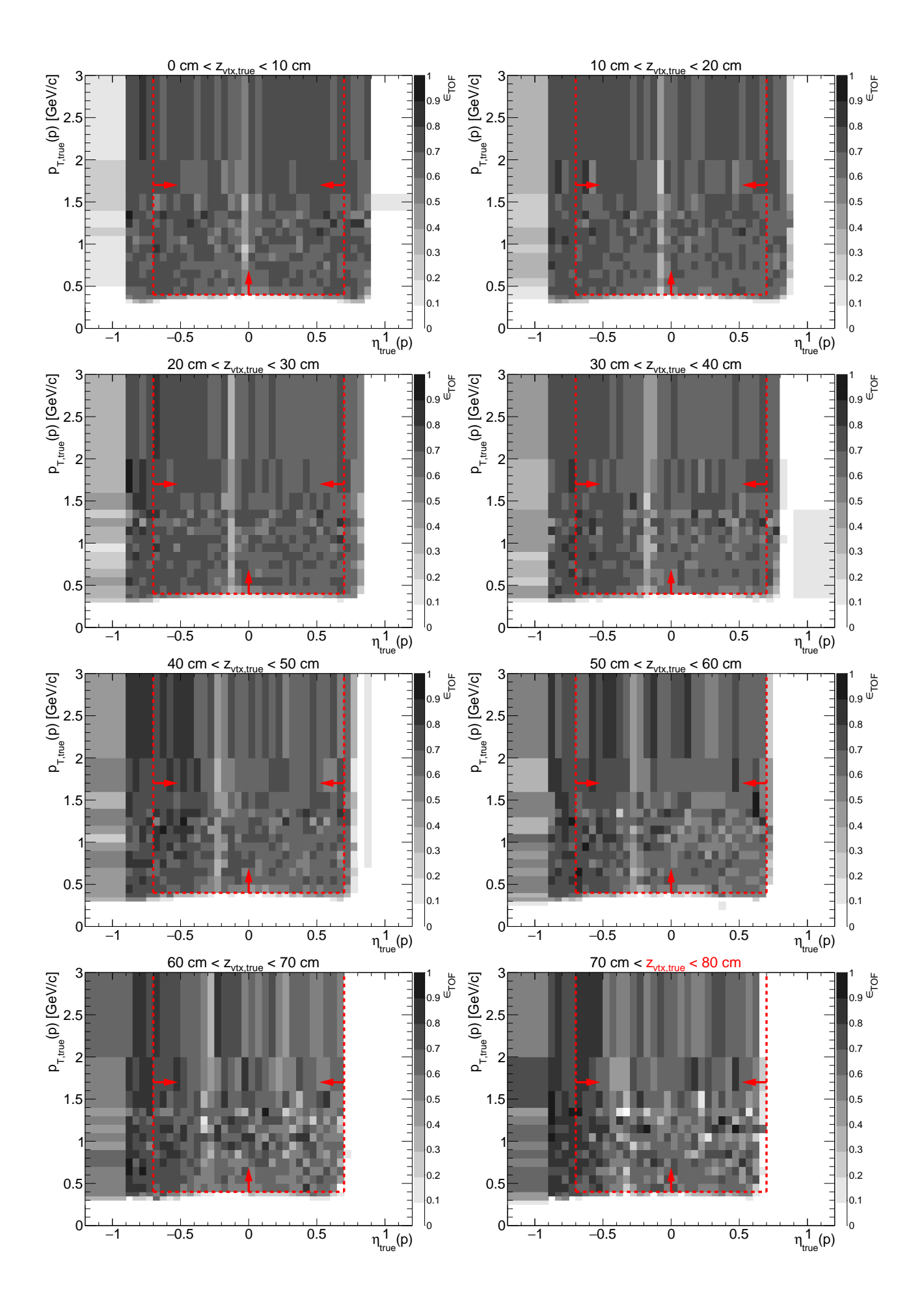


Figure 1.12: TOF acceptance, reconstruction and matching efficiency of p. Each plot represents the TOF efficiency  $\epsilon_{\text{TOF}}$  (z-axis) as a function of true particle pseudorapidity  $\eta$  (x-axis) and transverse momentum  $p_T$  (y-axis) in single z-vertex bin whose range is given at the top. Red lines and arrows indicate region accepted in analyses.





#### 1.3 TPC vertex reconstruction efficiency

The definition of vertex reconstruction efficiency established in this analysis is the probability that two global tracks, both associated with true-level primary particles from the kinematic region of the measurement, both satisfying kinematic and quality criteria (cuts ?? and ??) and both matched with hits in TOF, form a vertex listed in the collection of reconstructed primary vertices and DCA(R) and DCA(z) of both global tracks calculated w.r.t. this vertex is contained within the limits of cut ??.

## 2. Roman Pot simulation

### 3. dE/dx correction

Particle identification in our analyses is done using merged information from the TPC (specific energy loss of tracks dE/dx) and from the TOF (time of hit matched to TPC track). As can be seen in Fig. 3.3, dE/dx information from the MC events simulated in STARsim (in red) poorely matches the data points (black). This results e.g. in large systematic error of estimate of particle identification efficiency.

This problem was discussed under ticket #3272 (Ref. [3]). There were trials to improve the TPC calibration in simulation, but the problem remained. It was finally concluded that the origin of the problem lies in the model of energy loss used in the STARsim, therefore any further action was postponed.

In order to tune simulated reposponse of the TPC in terms of dE/dx, hence also reduce the systematic uncertainty related to particle identification, a correction method was developed based on proper transformation (recalculation) of simulated dE/dx to obtain new dE/dx whose distribution matches the data.

It is possible to transform dE/dx in MC to make it follow the shape of dE/dx in the data. We know that  $n_X^{\sigma}$  (where  $X = \pi, K, p, ...$ ) variable follows a gaussian distribution (for particle X)

$$n_X^{\sigma} = \left(\ln \frac{dE/dx}{\langle dE/dx \rangle_X}\right) / \sigma_{dE/dx}, \qquad f(n_X^{\sigma}) = \mathcal{N}(n_X^{\sigma}; \mu = 0, \sigma = 1)$$

therefore dE/dx itself follows log-normal distribution:

$$f(dE/dx) = \mathcal{L}og\mathcal{N}(dE/dx; \mu = \langle dE/dx \rangle, \sigma = \sigma_{dE/dx}) = \frac{1}{\sqrt{2\pi} \cdot \sigma \cdot dE/dx} e^{-\frac{\ln^2 \frac{dE/dx}{\langle dE/dx \rangle}}{2\sigma^2}}$$

The transformation we want to apply should preserve the shape of dE/dx (so that it is still described by  $\mathcal{L}og\mathcal{N}$ ), however it should change  $\mu$  and  $\sigma$  so that these values are eugal to those seen in the data. The transformation that satisfies above postulate is

$$dE/dx' = c \cdot (dE/dx)^a$$

Parameters of the distribution  $\mathcal{L}og\mathcal{N}(dE/dx')$  would be then

$$\mu' = c \cdot \mu^a, \quad \sigma' = a \cdot \sigma$$

From above we get formulae for parameters of the transformation:

$$a = \sigma'/\sigma, \quad c = \frac{\mu'}{\mu^a}$$

AlternativeToCrystallBall [4] Eq. (3.1)

$$f(dE/dx) = \begin{cases} \frac{A}{\sqrt{2\pi} \cdot \sigma \cdot dE/dx} \exp\left(-\frac{1}{2} \left(\frac{\ln \frac{dE/dx}{\langle dE/dx \rangle}}{\sigma}\right)^{2}\right) & \text{for } \frac{\ln \frac{dE/dx}{\langle dE/dx \rangle}}{\sigma} \leq k \\ \frac{A}{\sqrt{2\pi} \cdot \sigma \cdot dE/dx} \exp\left(-k \cdot \frac{\ln \frac{dE/dx}{\langle dE/dx \rangle}}{\sigma} + \frac{1}{2}k^{2} - k^{-1} \left(\frac{\ln \frac{dE/dx}{\langle dE/dx \rangle}}{\kappa} - 1\right)^{k}\right) & \text{for } \frac{\ln \frac{dE/dx}{\langle dE/dx \rangle}}{\sigma} > k \end{cases}$$
(3.1)

$$g(p) = P_1 + P_2 \cdot \exp(-P_3 \cdot p) + P_4 \cdot \arctan(P_5 \cdot (p - P_6))$$
 (3.2)

PID	$\langle dE/dx  angle_{ m Bichsel} - \langle dE/dx  angle_{ m MC}$					$\sigma (dE/dx)_{ m MC}$						
1 110	$P_1$	$P_2$	$P_3$	$P_4$	$P_5$	$P_6$	$P_1$	$P_2$	$P_3$	$P_4$	$P_5$	$P_6$
$\pi^{\pm}$	3.618e-8	5.838e-9	5.481				0.0809	-0.023	0.450	-7.84e-3	1.8489	1.04
$K^{\pm}$	-1.01e-10	-9.983e-6	7.581				0.0628	0.022	5.381	3.06e-3	7.3070	0.547
$p,ar{p}$	-4.041e-8	-1.179e-5	4.277				0.0660	0.082	12.042	1.07e-3	7.2872	0.889
$e^{\pm}$	-1.542e-7	3.393e-7	5.025				0.0572	0.982	37.984	2.61e-3	-27.995	0.693
$\overline{d}, \overline{d}$	-2.469e-6	0.3706	21.654	5.131e-7	30.050	0.781	0.1311	-0.971	4.691			

(a)													
PID		$\langle dE/dx  angle_{ m Bichsel} - \langle dE/dx  angle_{ m Data}$						$\sigma (dE/dx)_{ m Data}$					
	$P_1$	$P_2$	$P_3$	$P_4$	$P_5$	$P_6$	$P_1$	$P_2$	$P_3$	$P_4$	$P_5$	$P_6$	
$\pi^{\pm}$	-1.236e-8	1.777e-7	9.938				0.0738	16.86	39.44	-1.704e-3	6.482	0.628	
$K^{\pm}$	5.49e-10	-2.732e-6	7.712				0.0743	2.67e-5	7.17089				
$p,ar{p}$	-2.140e-7	0.0421	48.305	7.512e-8	15.544	0.575	0.0779	1.822	22.4277				
$e^{\pm}$	6.701e-8	3.304e-7	7.845				0.0678	468.9	59.4001				
$d, ar{d}$	-1.631e-7	0.0818	18.91				0.1259	-0.288	3.28733				
						(b)							

Table 3.1: Parameters of functions from Fig. 3.2 describing track dE/dx as a function of reconstructed momentum for a few particle species. Units of parameters  $P_i$  are such that if one provides momentum in Eq. (3.2) in GeV/c the resultant offset of dE/dx MPV with respect to Bichsel parametrization is in GeV/cm, and the resultant  $\sigma$  parameter is unitless.

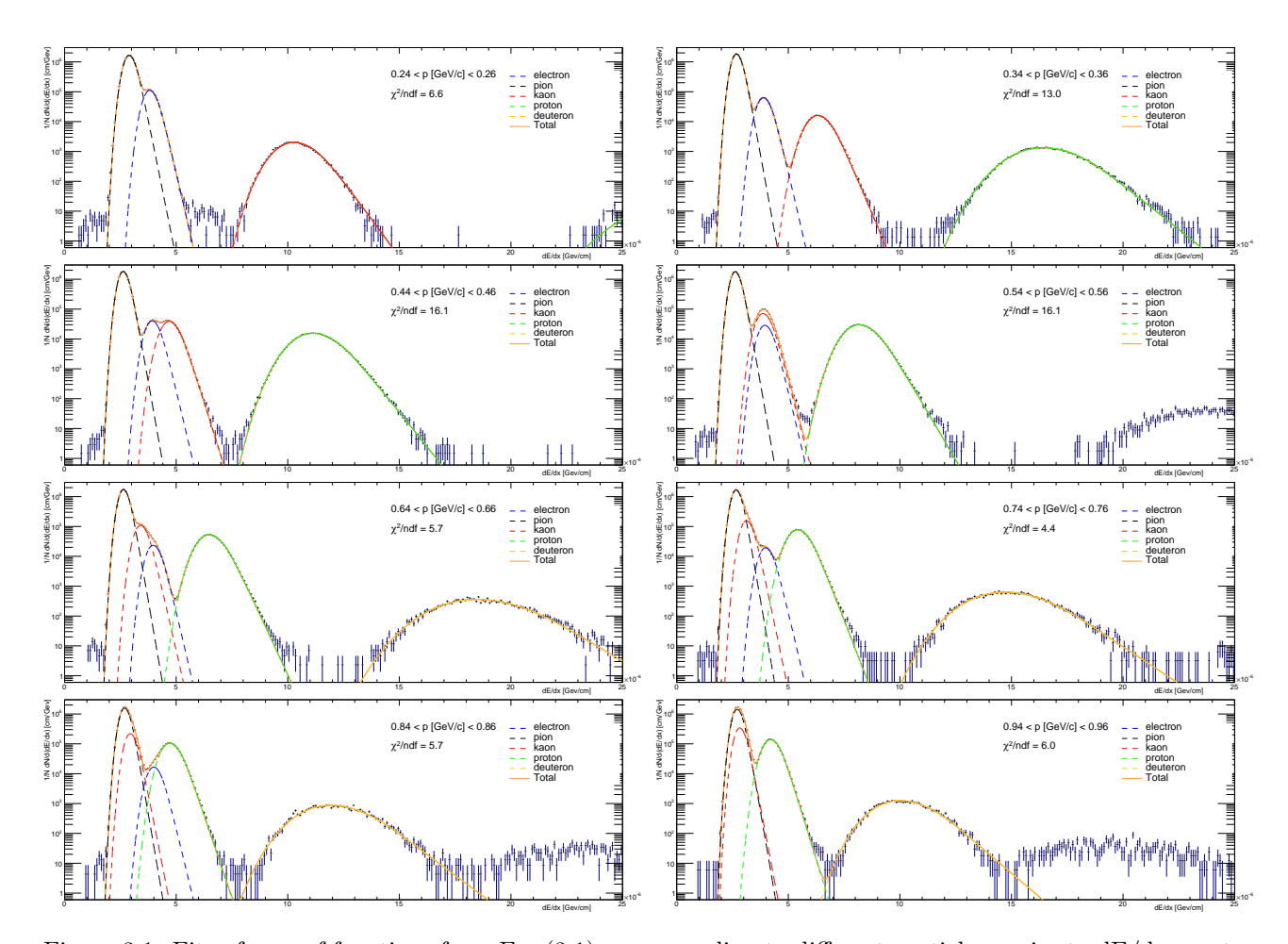


Figure 3.1: Fits of sum of functions from Eq. (3.1) corresponding to different particle species to dE/dx spectra from the data in a few momentum bins.

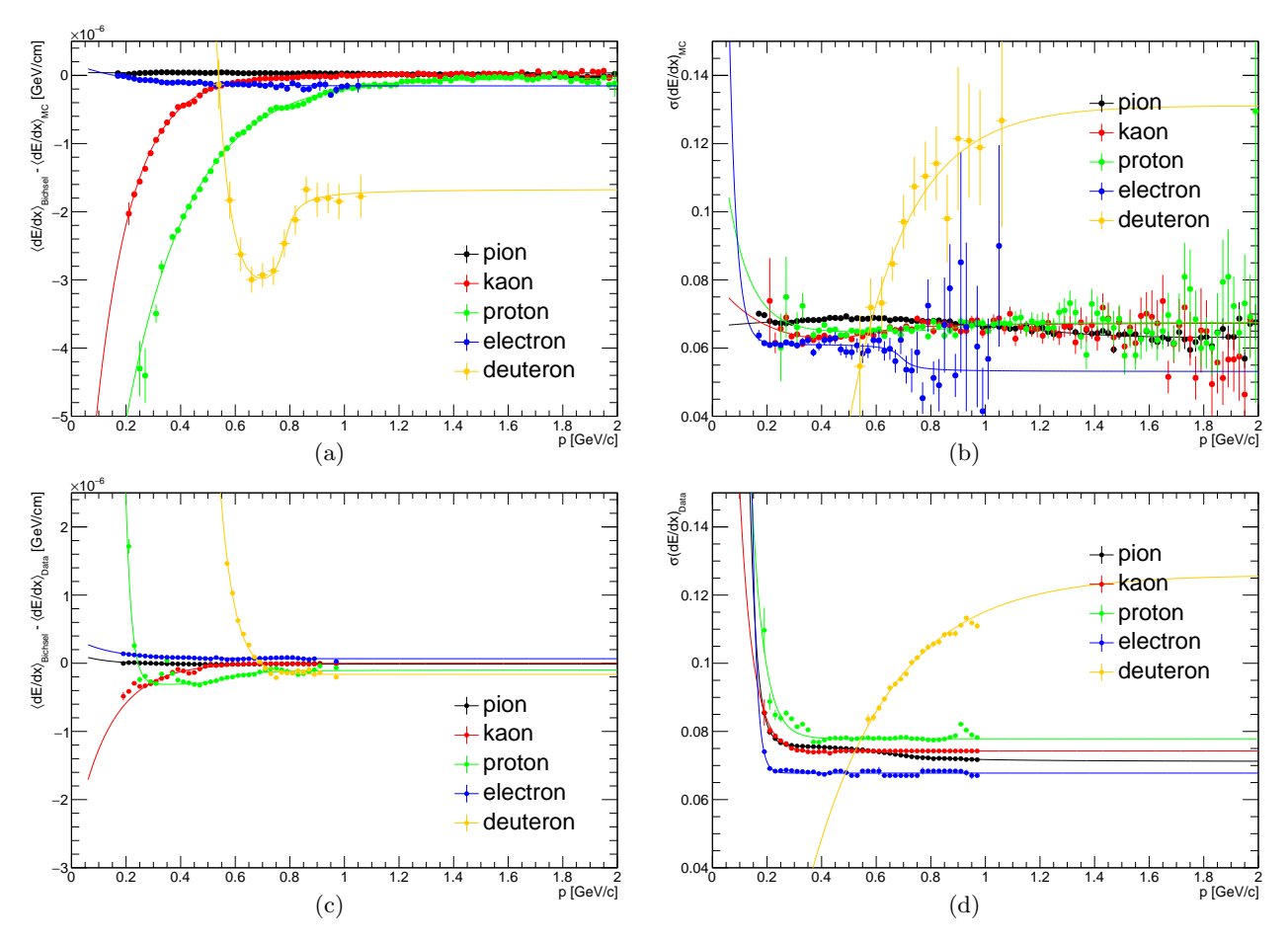


Figure 3.2: Difference between MPV of dE/dx predicted by Bichsel parametrization and obtained from the fit of Eq. (3.1) to dE/dx distribution in the data (3.2c) and MC sample (3.2a) and dE/dx width parameter in data (3.2d) and MC (3.2b) as a function of reconstructed particle momentum for a few particle species. Solid lines represent fits to points of corresponding color.

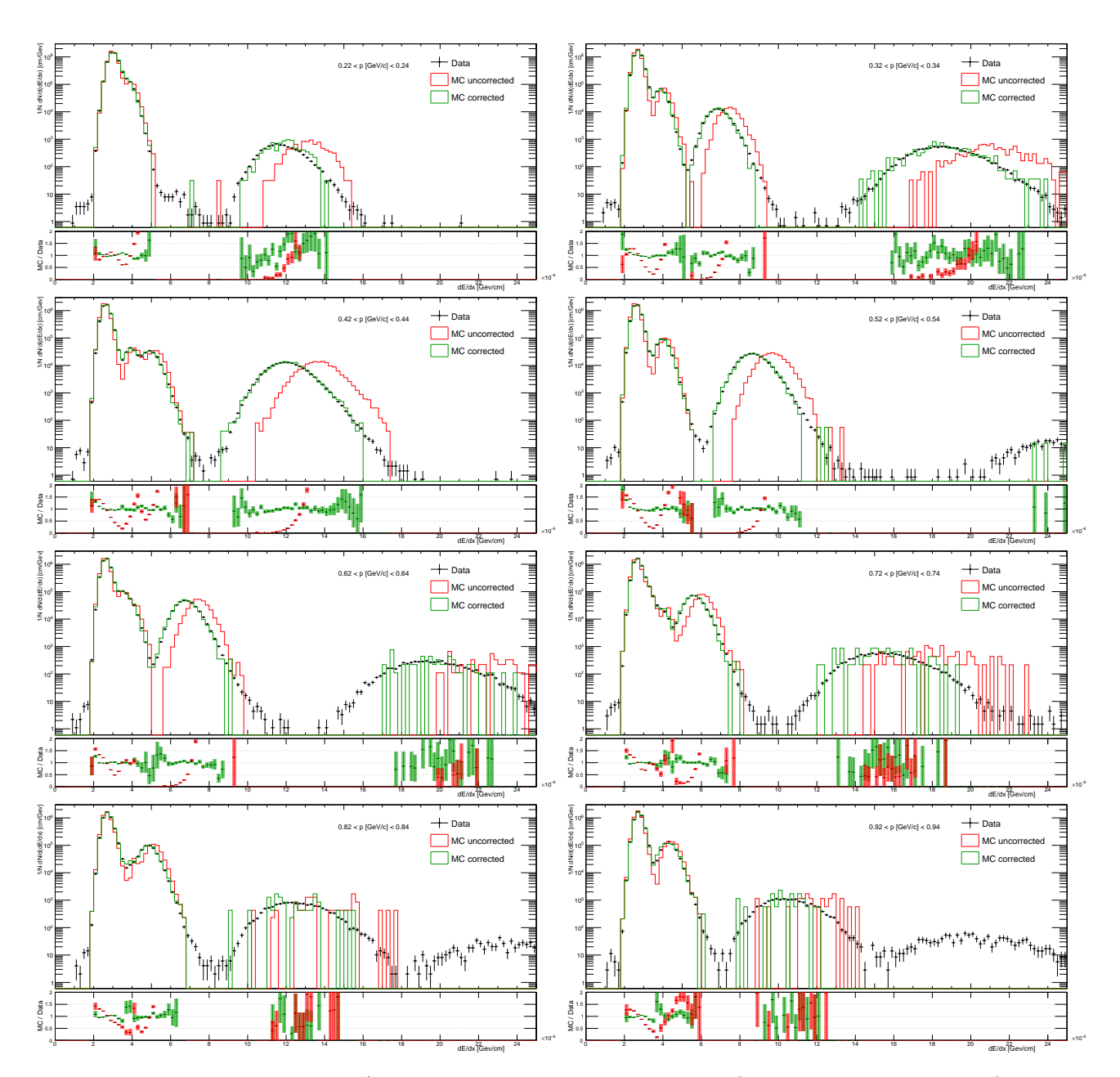


Figure 3.3: Comparison of the dE/dx spectra between the data and MC (before and after correction) in a few momentum bins.

# 4. TPC track pointing resolution adjustment

It was found during the analysis that distributions of quantities which describe the pointing resolution of the TPC tracks do not agree well between the data and embedded MC. Namely, the resolutions of the global helices associated with the tracks were found to be significantly better in the STAR simulation than in the data, what manifests as narrower DCA and  $d_0$  distribution in the embedded MC, comparing to corresponding distribution in the data (Fig. 4.5). This issue was discussed under ticket #3332 (Ref. [5]).

This problem could affect the momentum resolution and thus all other resolutions and reponse matrices used in data unfolding. Therefore the resolution adjustment procedure was performed to find appropriate parameters of the "artificial" helix deterioration and finally obtain agreement between DCA and  $d_0$  distributions (and all related resolutions) in the data and embedded MC.

In order to reduce pointing resolution in the MC an additional smearing of the helix radius  $\sigma(R)$  was introduced. Based on  $d_0$  comparison in Fig. 4.5a it was decided to account also for the systematic bias of the helix radius  $\Delta\mu(R)^1$ , which may be present e.g. due to differences in the material budget used the simulation and reconstruction. Both smearing and bias of the helix radius were introduced only for MC tracks which were matched with the true-level particles since only simulated tracks require adjustment (tracks from zero-bias event used in embedding already contain all detector effects).

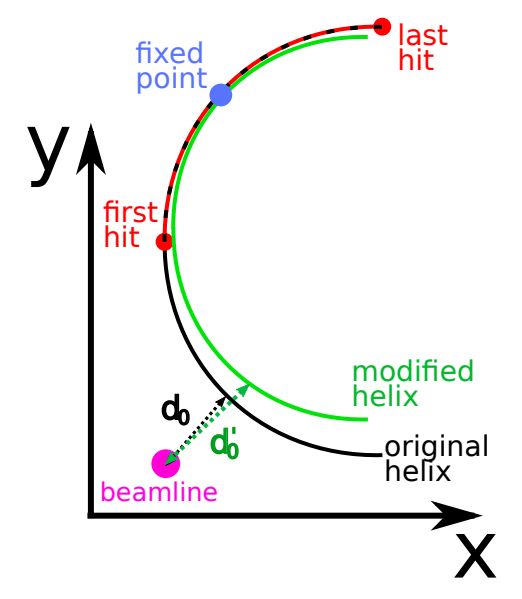


Figure 4.1: Sketch of helix modification procedure and  $d_0$  calculation.

Extraction of  $\Delta\mu(R)$  and  $\sigma(R)$  parameter required to achieve agreement of pointing resolution between embedded MC and the data involved a few steps, as listed below:

- 1. Series of  $d_0$  histograms in bins of  $p_T$  (100 MeV/c wide) was prepared, each for different size of distortion (different  $\Delta\mu(R)$  and  $\sigma(R)$ ) of global helix of the TPC tracks matched with true-level particles (example plot in single  $p_T$  bin is shown in Fig. 4.2):
  - (a) for each set of parameters  $\Delta\mu(R)$  and  $\sigma(R)$  the helix radius R was recalculated independently for each track following the Eq. (4.1):

$$R' = R \times \mathcal{N} \Big( 1 + \Delta \mu(R), \ \sigma(R) \Big),$$
 (4.1)

(b) new helix of a radius R' was assigned to a track and used to calculate  $d_0$ . The modified helix was obtained by changing the radius of original helix from R to R' with a fixed middle point between the first and last TPC hit of a global track represented by the helix (Fig. 4.1). The momentum of the track was also recalculated:

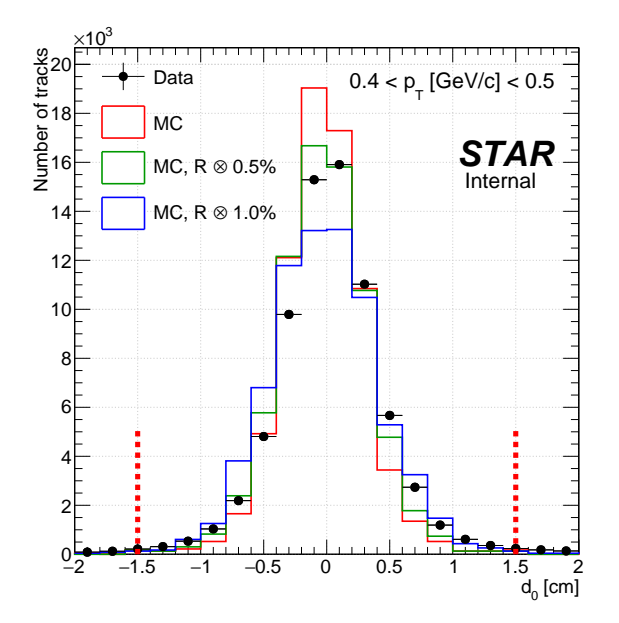
of the track was also recalculated:  

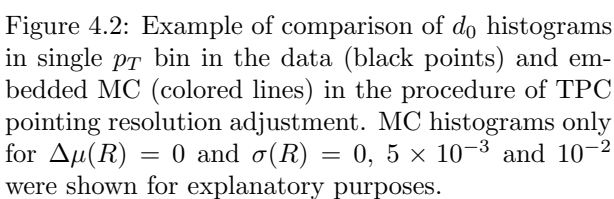
$$p_T' = p_T \times \frac{R'}{R}, \qquad \eta' = \eta \times \frac{R'}{R}. \tag{4.2}$$

- 2. In each  $p_T$  bin the  $\chi^2/\text{NDF}$  was calculated between the data and MC  $d_0$  histogram in a range -1.5 cm  $< d_0 < 1.5$  cm (corresponding to  $d_0$  cut used in analyses), for every point in parameter space of radius distortion (for every set of  $\Delta\mu(R)$  and  $\sigma(R)$ ). An example (single  $p_T$  bin) of map of  $-\chi^2/\text{NDF}$  in a parameter space is presented in Fig 4.3.
- 3. In each bin of recalculated  $p_T$  the 2-dim parabola  $z(x, y; a, b, x_0, y_0, z_0)$  given in Eq. (4.3)  $(z = \chi^2/\text{NDF}, x = \Delta\mu(R), y = \sigma(R))$  was fitted to  $-\chi^2/\text{NDF}$  in the global minimum region to obtain the best-fit distortion parameters.  $z = z_0 a(x x_0)^2 b(y y_0)^2. \tag{4.3}$

4. The best-fit smearing  $\sigma(R)$  (equal to parabola parameter  $y_0$ ) and best-fit bias  $\Delta\mu(R)$  ( $x_0$ ) from individual  $p_T$  bins was plotted as a function of global track  $p_T$  (Fig. 4.4). Each point was assigned with an error being a quadratic sum of two components: the error on  $x_0$  ( $y_0$ ) resulting from the parabola fit to  $-\chi^2/\text{NDF}$ , and length of corresponding semi-axis of ellipsis formed by the intersection of fitted parabola with the xy-plane at  $z = z_0 - 1/\text{NDF}$  (from definition of the parameter uncertainty given by the change of overall  $\chi^2$  by 1 unit). Resultant formulae for the error of each individual point in Fig. 4.4 are

Transverse impact parameter  $d_0$  takes positive value if the beamline is contained inside the helix (in the yz-plane projection), otherwise it is negative. Any asymmetry in the  $d_0$  distribution in the MC with respect to the data indicates presence of systematic difference in reconstructed  $d_0$ , hence also in reconstructed R.





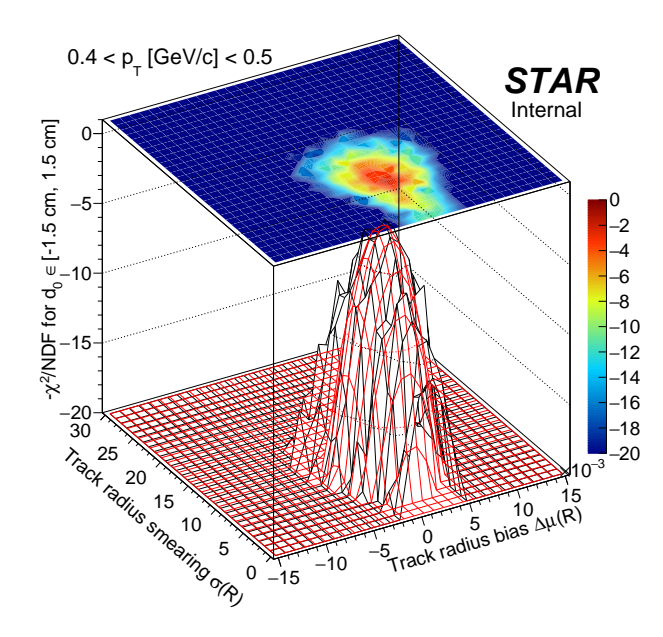


Figure 4.3: Example of  $-\chi^2/\text{NDF}$  map in a parameter space in the procedure of TPC pointing resolution adjustment. The red surface represents parabola fitted in the vicinity of the global minimum.

$$\delta\left(\Delta\mu(R)\right) = \sqrt{\delta_{\rm fit}^2(x_0) + \frac{1}{2b{\rm NDF}}},\tag{4.4}$$

$$\delta\left(\sigma(R)\right) = \sqrt{\delta_{\rm fit}^2(y_0) + \frac{1}{2b{\rm NDF}}}.\tag{4.5}$$

From Fig. 4.2 one can read that NDF = 14. In calculation of uncertainties correlation of  $\Delta\mu(R)$  and  $\sigma(R)$  have not been accounted.

5. The empirically determined functions were fitted to points representing  $\Delta \mu(R)$  and  $\sigma(R)$  dependence on the global track  $p_T$ . Their form and values of parameters are given in Fig. 4.4.

Helices of global TPC tracks were deteriorated according to Eq. (4.1) and the parametrizations of global track  $p_T$ -dependence of  $\Delta\mu(R)$  and  $\sigma(R)$  from Fig. 4.4, to verify if better agreement between the data and embedded MC is found after the adjustment. Filled histograms in Fig. 4.5 show  $d_0$  and DCA distributions after the described adjustment, and filled circles in the bottom pad show their ratio to the data points. Clearly, there is much better agreement between embedded MC and the data after the pointing resolution adjustment. Remaining differences may arise from incomplete theoretical model of the CEP process impleneted in GenEx leading to different  $p_T$  spectra of the data and the model (e.g. model does not contain resonant  $\pi^+\pi^-$  production).

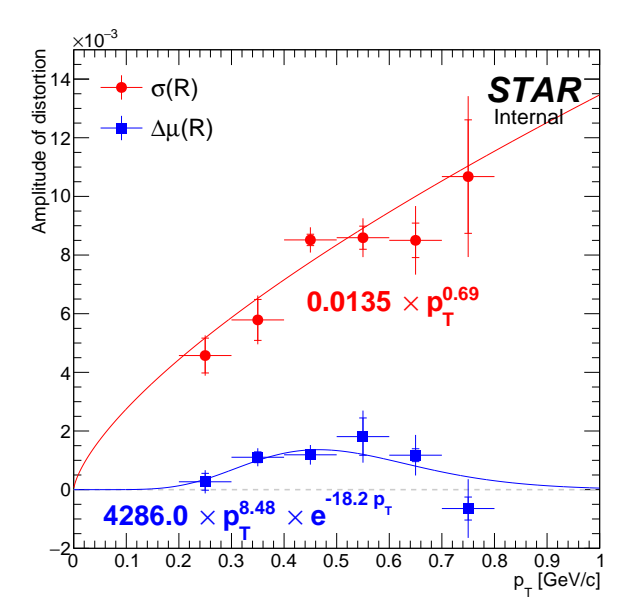
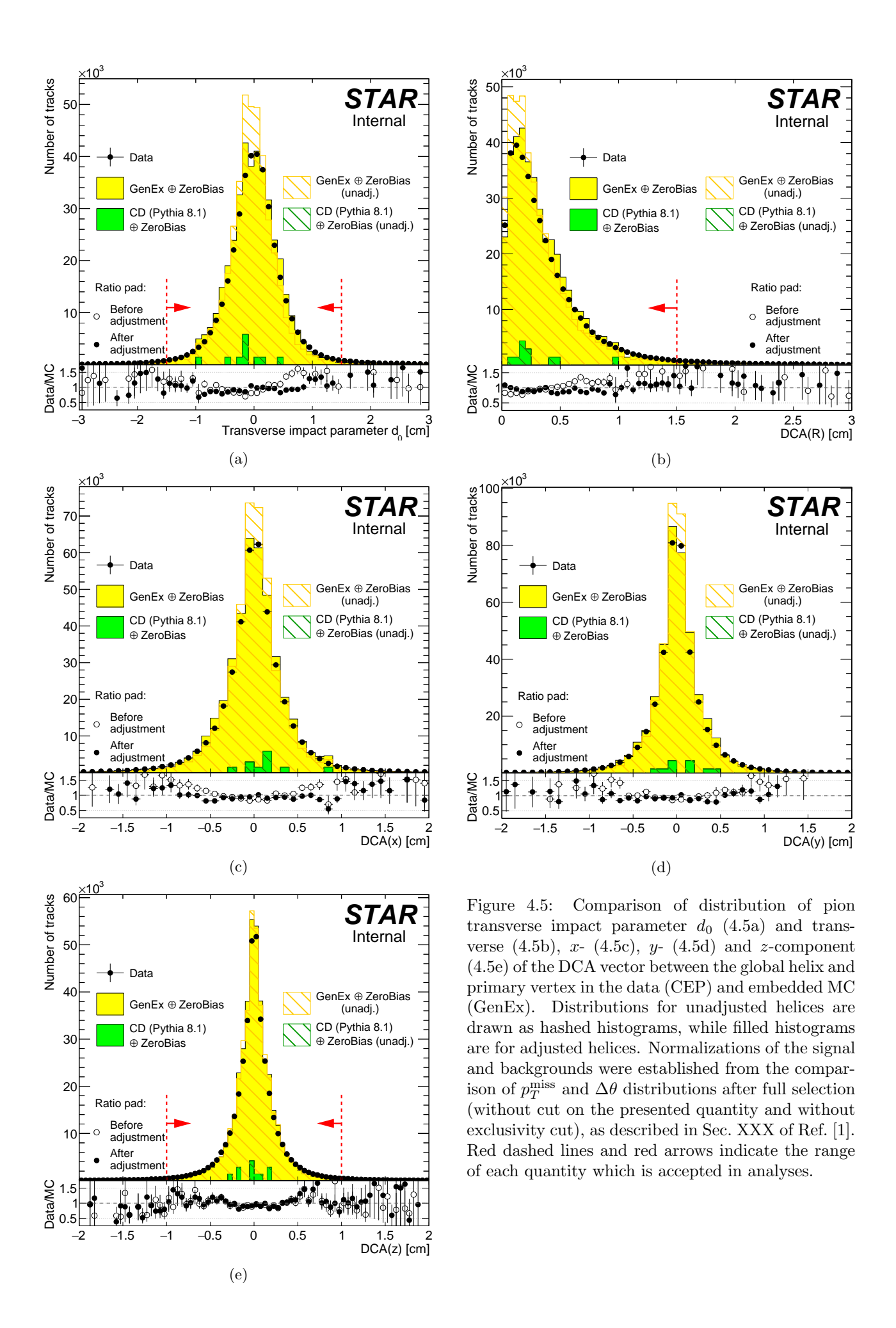


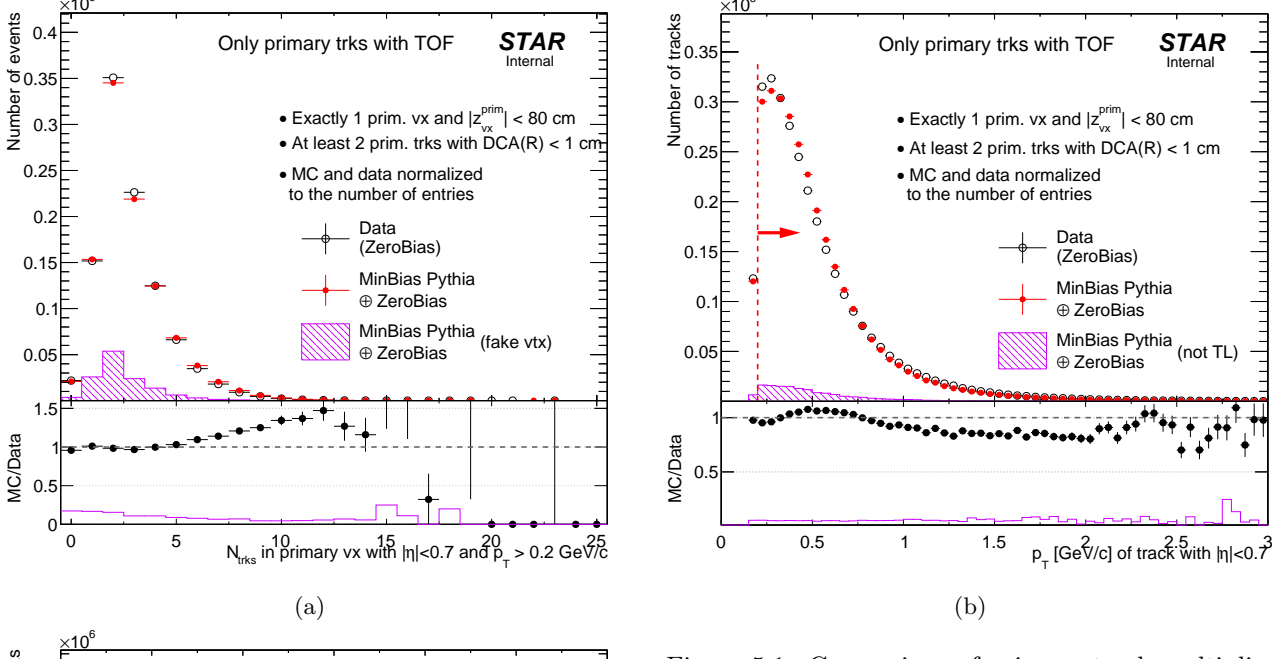
Figure 4.4: Best-fit parameters obtained in the procedure of the TPC track pointing resolution adjustment. Uncertainties on parameters resulting solely from the fit of Eq. (4.3) to  $-\chi^2/\text{NDF}$  are represented by the lines with perpendicular endings. Total uncertainties (Eqs. (4.4), (4.5)) extend beyond. The empirical functions fitted to points are drawn with corresponding colors, and formula of each is written aside.



#### 5. Dead material in front of TPC

Particle detected and reconstructed in the TPC must first pass through the detector material standing in between the accelerator vacuum and TPC gas. This affects track reconstruction efficiency, as the particle may interact with that material - in worst case inelastically, and induce secondary particles thus lower reconstruction efficiency. Accuracy of modeling of the detector material in the STAR simulation, especially in run 15 with the HFT installed, influences systematic error e.g. on the TPC track reconstruction efficiency. In this section the density of secondary vertices is compared between the data and embedded MC. The density of secondary vertices is directly propotional to the amount of the material in given volume, hence any discrepancy between secondary vertex distribution in the data and MC can be a hint for innacuracies of the STAR simulation which should be accordingly covered by the systematic uncertainties. It should be stressed that this analysis is not aimed to tune the material budget in the STAR simulation, as there are much better data for this than high-luminosity proton-proton collisions from run 15. The aim of presented study is to obtain reasonable estimate of the component of systematic uncertainty of the TPC track reconstruction efficiency related to the error on the amount and distribution of simulated material.

Analysis of the distribution of secondary vertices was performed using both zero-bias (ZB) data and minimumbias MC (Pythia) embedded into zero-bias triggers. Because of insufficient statistics of the ZB data, for the purpose of analysis presented in this section both standard ZB data sample (from ZB triggers in st\_rp stream) and the subsample of RP\_CP triggers (see Ref. [6] for trigger details) with identified elastic proton-proton scat-



Number of tracks STAR Only primary trks with TOF • Exactly 1 prim. vx and lz l < 🕅 cm 0.08 At least 2 prim. trks with DCA(R) < 1 cm MC and data normalized to the number of entries 0.06 Data (ZeroBias) 0.04 MinBias Pythia ⊕ ZeroBias 0.02 MinBias Pythia (not TL ⊕ ZeroBias MC/Data -1.5 -0.5 0  $\eta$  of track with p\_>0.2 GeV/c (c)

Figure 5.1: Comparison of primary track multiplicity (5.1a),  $p_T$  (5.1b) and  $\eta$  (5.1c) distribution in zero-bias data and minimum-bias MC embedded into zero-bias triggers. In all subfigures MC histogram is normalized to have the same integral as the data histogram. Violet hashed histogram in Fig. 5.1a represents the fake vertices defined as vertices of which less than a half of constituent tracks is matched to truelevel particles. Violet hashed histogram in Fig. 5.1b and 5.1c represents tracks not matched to true-level particles. Bottom pads in each figure show the ratio between MC and data as black points, and the ratio between fake (violet histogram) and all MC entries (red points) as a violet line. Red dashed lines and arrows indicate range of tracks required in selection of events for the secondary vertex analysis.

tering events using loose RP track selection were used. The latter subsample is in good approximation a ZB sample in terms of central detector, as it was triggerd only by the east and west coincidence of Roman Pots any particles present in the TPC and TOF must be product of pile-up interaction. In all plots and later in the text we refer to this merged sample as ZB data sample.

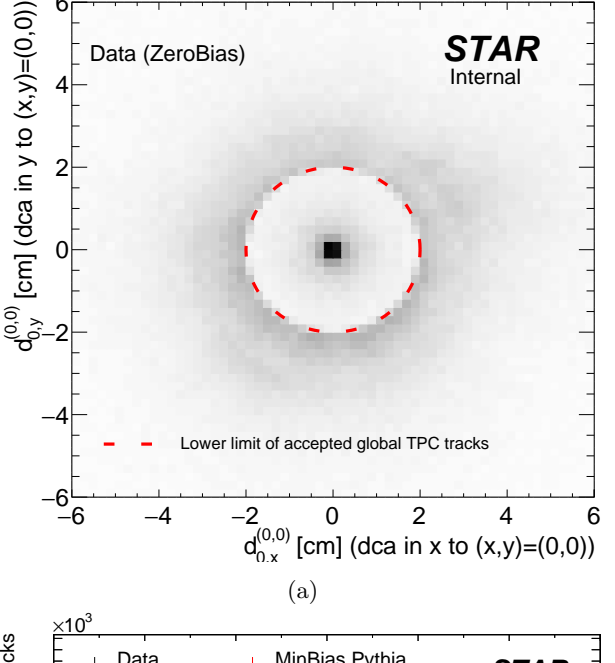
Analysis started with the following selection of events:

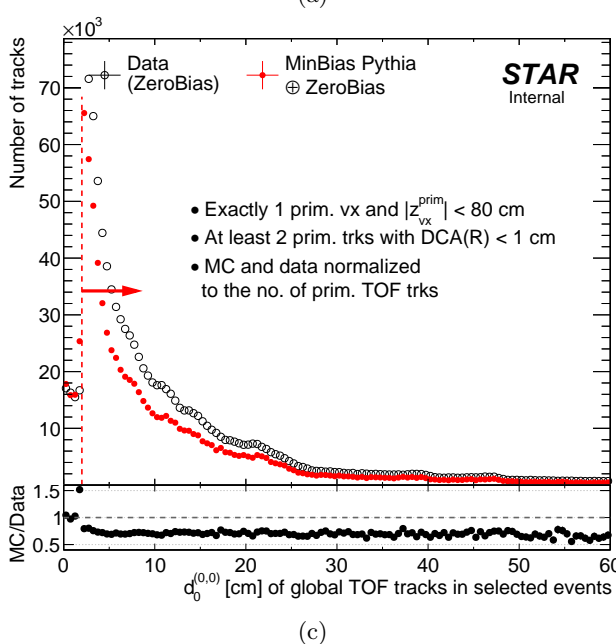
- 1. Exactly 1 reconstructed primary vertex (with tracks matched to hits in TOF),
- 2.  $|z_{vx}| < 80$  cm,
- $$\begin{split} & \text{DCA(R)} < 1 \text{ cm}, & |\eta| < 1, & p_T > 0.2 \text{ GeV}/c, \\ & N_{\text{hits}}^{\text{fit}} \geq 25, & N_{\text{hits}}^{\text{dE/dx}} \geq 15, & N_{\text{hits}}^{\text{fit}}/N_{\text{hits}}^{\text{poss}} \geq 0.52. \end{split}$$
  3.  $\geq 2$  prim. TOF tracks with:

The aim of above criteria was to select pile-up-free events with well defined vertex. Cut on z-vertex is identical to one used in physics analyses. Figure 5.1 shows comparison of quantities characterizing an event. In general a moderate agreement between MC and data can be observed, considered sufficient for trustworthy result of described analysis.

As a next step the TPC tracks were selected for the search and reconstruction of secondary vertices. The requirements were as follows:

- 1. Global TPC tracks matched with TOF not associated with any primary TPC track,
- 2.  $|\eta| < 0.7$ ,  $p_T > 0.2 \text{ GeV}/c$ ,  $N_{\text{hits}}^{\text{fit}} \ge 25$ ,  $N_{\text{hits}}^{\text{dE/dx}} \ge 15$ ,  $N_{\text{hits}}^{\text{fit}}/N_{\text{hits}}^{\text{poss}} \ge 0.52$ , 3. Distance of closest approach to the STAR z-axis (x, y) = (0, 0),  $d_0^{(0, 0)}$ , larger than inner radius of the beampipe:  $d_0^{(0,0)} > 2$  cm.





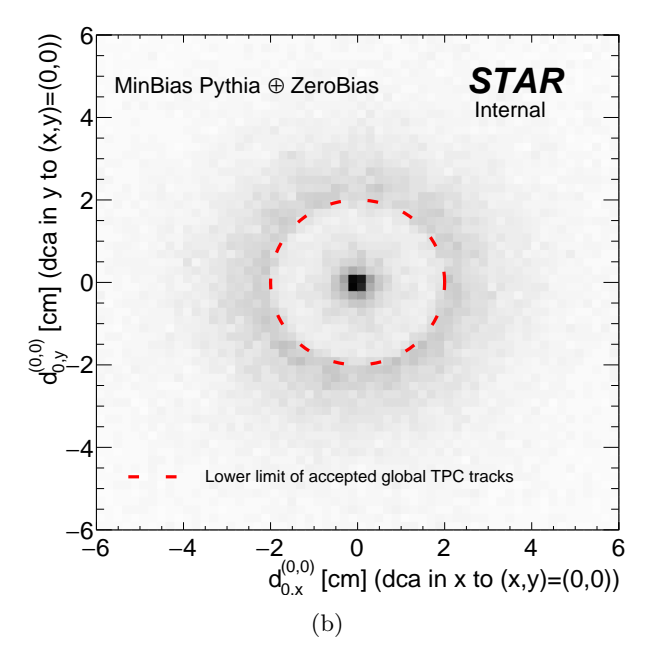


Figure 5.2: Two-dimensional  $d_0^{(0,0)}$  distribution of global TPC tracks matched with TOF in zero-bias data (5.2a) and embedded minimum-bias MC (5.2b), and comparison of their radial projection in wider range of  $d_0^{(0,0)}$  (5.2c). Red dashed lines and arrow indicate limit of  $d_0^{(0,0)}$  of tracks accepted for the secondary vertex analyses (limit equals 2 cm). In all subfigures there are only entries from global tracks not associated with the primary tracks. Even with relatively low pointing resolution of the TPC tracks  $(\sim 1 \text{ cm})$  one can recongnize structures which can be attributed the beampipe starting at  $d_0^{(0,0)} = 2$  cm, and HFT elements at about 8 cm, 11 cm, 14 cm and 22 cm.

These cuts were intended to select in-time TPC tracks with high chance of being a product of secondary interaction of primary particle with the detector material. The higher limit of accepted  $d_0^{(0,0)}$  was set in analysis, the less background was found in the secondary vertex distribution for a price of limited access to secondary vertices of low radial distance from STAR z-axis. Cut of 2 cm was found a good compromise. In Fig. 5.2 we present comparison of  $d_0^{(0,0)}$  distribution of selected global TOF-matched TPC tracks in the data and embedded MC (without cut on  $d_0^{(0,0)}$ ). To some extent this distribution reflects the material density (secondary vertex density) in the radial direction, therefore we present it with the MC distribution normalized to the same total number of primary tracks as in the data. Number of secondary vertices is proportional to the number of primary particles, so we use such normalization to allow direct comparison of the distributions:

$$\text{MC normalization factor} = \frac{\langle N_{\text{trks/evt}}^{\text{DATA}} \rangle \times N_{\text{evts}}^{\text{DATA}}}{\langle N_{\text{trks/evt}}^{\text{MC}} \rangle \times N_{\text{evts}}^{\text{MC}}} = \frac{N_{\text{trks}}^{\text{DATA}}}{N_{\text{trks}}^{\text{MC}}}$$
 (5.1)

Especially in Fig. 5.2c one can find structures/peaks that might be attributed to subdetectors (PXL, IST, SST) of the HFT. Notable is different yield of histograms which could indicate different amount of simulated dead material with respect to real conditions. The reason of this inconsistency was found in imperfect simulation of the pointing resolution of the TPC tracks - because the resolution is higher in the simulation, more true primary tracks is reconstructed as primary tracks hence less such tracks is accepted in the global track selection (comparing to data). This effect is accounted later in the background subtraction procedure.

After secondary track candidates were selected, the described algorithm for secondary vertex reconstruction was used:

- 1. Loop over all pairs of secondary track candidates, store pairs whose DCA is less than 0.5 cm (nearby tracks passing a proximity cut),
- 2. Link pairs of nearby tracks into sets of tracks connected by the common nearby tracks,
- 3. Loop over all sets defined in 2., in each set loop over all pairs from given set, reject worst-matching tracks (these with largest DCA to others) until all pairs of tracks have DCA less than 0.5 cm,
- 4. Based on number of tracks in secondary vertex, total charge, specific energy loss, dE/dx, cosine of the opening angle of two tracks  $cos(\theta)$  and invariant mass of two tracks  $m_{\rm inv}$  determine if the vertex is from resonance decay or photoconversion (see Ref. [7]); if none of the two then assume hadronic vertex,
- 5. Calculate the vertex position as the average DCA point of all track pairs in the vertex.

As a result secondary vertices were reconstructed, whose multiplicity distribution is depicted in Fig. 5.3. Analysis was continued only with vertices of multiplicity

equal 2. The first reason was that most of vertices consist is ribution pair of tracks. Another reason was the background subtraction method developed only for vertices made of two tracks. In addition to this, only vertices representing primary particles in the pseudorapidity range  $-0.7 < \eta < 0.7$  were analyzed. To enable such selection a variable  $\eta_{\rm vtx}$  was defined, as shown in Fig. 5.4.

Raw distributions of  $R_{\rm vtx}^{\rm secondary}$  and  $z_{\rm vtx}^{\rm secondary}$  are shown in Fig. 5.5a and Fig. 5.5b, respectively. In  $R_{\rm vtx}^{\rm secondary}$  spectrum one can find peaks in the regions where the HFT subdetectors are placed. Peaks seem to lie on top of a

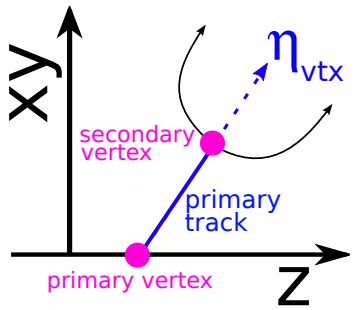


Figure 5.4:  $\eta_{\text{vtx}}$  definition (sketch).

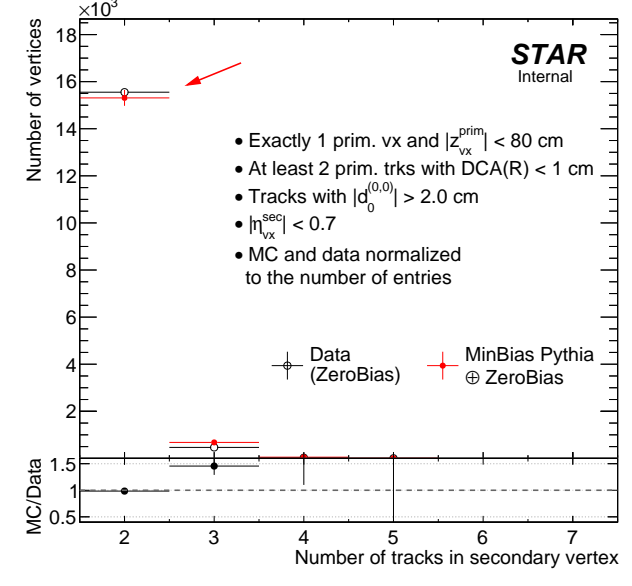


Figure 5.3: Multiplicity of tracks in reconstructed

secondary vertices. Red arrow points to bin with

vertices used in final comparisons of vertex position

Raw distributions of  $R_{\rm vtx}^{\rm secondary}$  and  $z_{\rm vtx}^{\rm secondary}$  are shown in Fig. 5.5a and Fig. 5.5b, respectively. In  $R_{\rm vtx}^{\rm secondary}$  spectrum one can find peaks in the regions where the HFT subdetectors are placed. Peaks seem to lie on top of a tail whose origin has been identified with the secondary vertices made of pairs containing true primary tracks which were not associated with any primary vertex and unfortunately passed selection of global tracks for the secondary vertex reconstruction. Without this backgroud subtracted, the ratio of MC to data varies mostly between 0.5 and 0.7. For this reason a method of estimation of

Background estimation makes use of different content of fake secondary vertices depending on the proximity cut used in the secondary vertex reconstruction. Figure 5.6 shows the percentage of backgroud (fake pairs) distributed over the distance of closest approach between two tracks. A comment needs to be

the backgroud was invented, as described in the next paragraph.

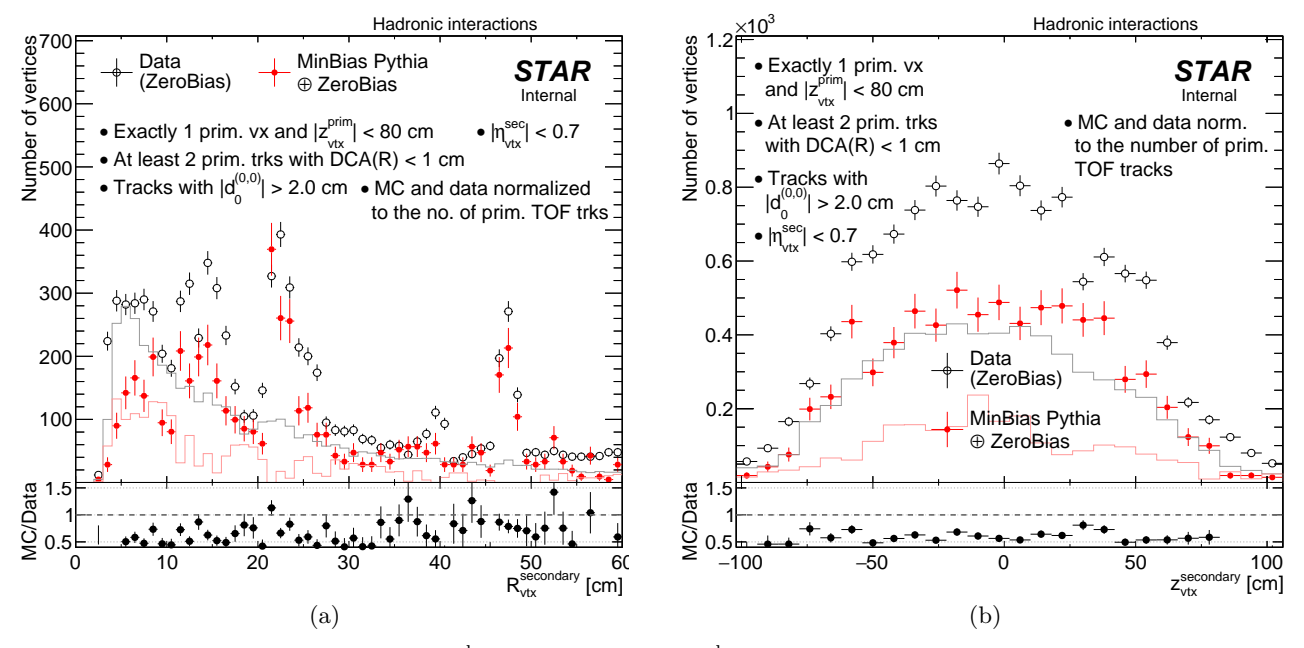


Figure 5.5: Comparison of raw  $R_{\rm vtx}^{\rm secondary}$  (5.5a) and  $z_{\rm vtx}^{\rm secondary}$  (5.5b) distribution in the data (opened black circles) and embedded MC (filled red circles). Only vertices recognized as products of hadronic interactions are shown in the figure. Solid lines denote estimated backgroud content in the distribution of corresponding color.

made that the agreement of the shape of the tails in data and MC distributions was achieved only after the adjustment of the TPC resoltion in MC, as described in Sec. 4. This agreement allows to believe in proper description of the data by MC in terms of backgroud distribution over DCA of two global tracks, which is used in the backgroud estimation.

It agrees with intuition that the most optimal cut to select pairs from the secondary vertices is as low as about 0.5 cm, however one can select sample with slightly different ratio of signal to background if the proximity cut is changed to accept tracks of DCA within some higher limits. In Fig. 5.6 the nominal proximity cut is

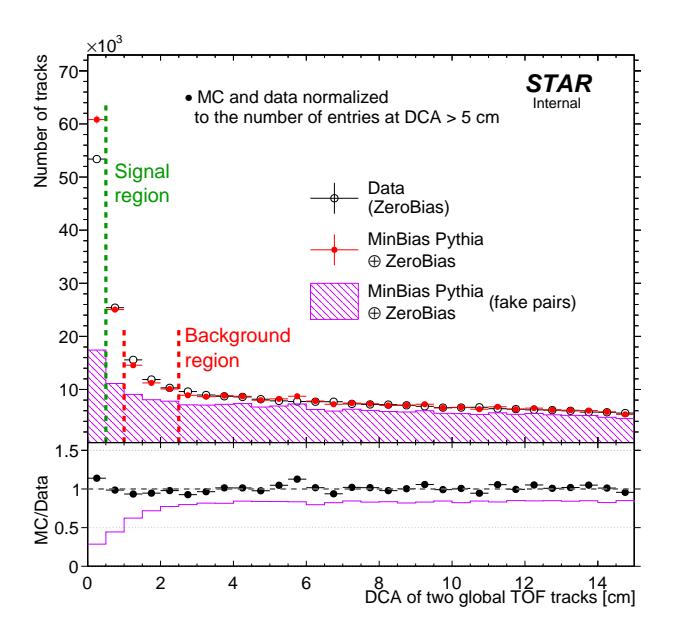


Figure 5.6: Comparison of DCA between all pairs of secondary track candidates selected for the secondary vertex reconstruction in the data and embedded MC. MC histogram is normalized to the data at DCA > 5 cm. Violet hashed histogram depicts pairs contained in MC histogram and not originating from the same vertex. Solid violet line in the lower pad denotes ratio of violet and red histogram.

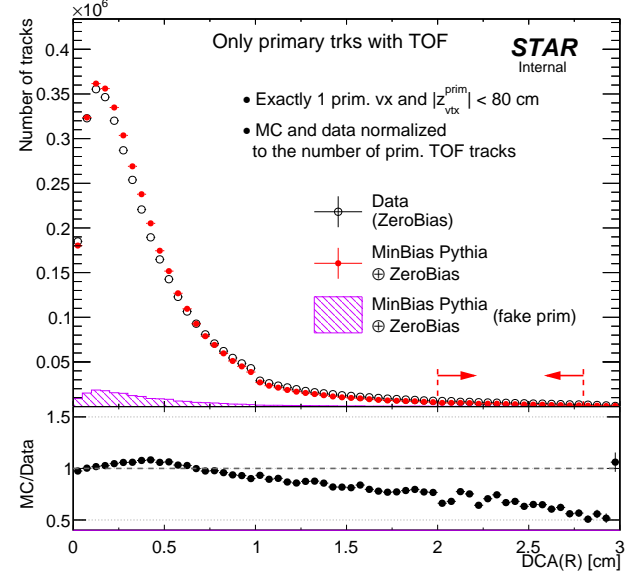


Figure 5.7: Comparison of radial DCA of all primary tracks matched with TOF and passing quality criteria in events selected for secondary vertex analysis, between the data and embedded MC. Violet hashed histogram represents tracks not matched to true-level particles. Red dashed lines and arrows limit region used to find normalization that compensates different backgroud yield in reconstructed secondary vertex distributions in data and embedded MC.

marked with the green line (signal region), while the modified proximity cut is marked with red lines (backgroud region). With such two versions of cuts used in vertexing the two independent distributions of secondary vertices can be obtained: one with the standard proximity cut -  $\mathcal{H}_1$ , the other with modified proximity cut, in our case 1.0 cm < DCA < 2.5 cm -  $\mathcal{H}_2$ . Limits in modified proximity cut were set to such values in order to ensure enough statistics as well as provide satisfactory resolution of secondary vertex position calculated as a middle point between DCA points on helices associated with the tracks. One can note that the content of histograms can be described by the set of equations given below:

$$\begin{cases}
\mathcal{H}_1 = (1 - B) \times \text{signal} + B \times \text{backgroud}, \\
\mathcal{H}_2 = (1 - B') \times \text{signal} + B' \times \text{backgroud},
\end{cases}$$
(5.2)

in which parameters B and B' denote the backgroud fraction in the distribution resultant from analysis utilizing nominal and modified proximity cut, respectively. The solution to set of Eqs. (5.2), (5.3) is the following:

$$\begin{cases}
signal = \frac{B' \times \mathcal{H}_1 - B \times \mathcal{H}_2}{B' - B} \\
backgroud = \frac{(1 - B) \times \mathcal{H}_2 - (1 - B') \times \mathcal{H}_1}{B' - B}
\end{cases} (5.4)$$

An important remark here is that the backgroud fraction extracted from the ratio of violet and red histograms in Fig. 5.6 can be used directly in Eqs. (5.2)-(5.5) only for backgroud estimation in MC. In case of background estimation in data parameters B and B' have to be corrected for the leakege of true primary tracks to set of selected secondary track candidates, as it was decribed in one of preceding paragraphs. The correction factor  $\kappa$  is extracted from the ratio of the radial DCA of the primary TPC tracks in events selected for the secondary vertex study. Histogram range selected for calculation of the ratio was set to 2.0 cm < DCA(R) < 2.6 cm, as this range coincides with the  $d_0^{(0,0)}$  of global tracks accepted for the analysis.  $\kappa$  calculated in this range equals 1.48. Variation of value of  $\kappa$  with changed limits of DCA(R) selected for the ratio calculation do not influence significantly the final result. The correction is done by multiplying fraction B and B' by  $\kappa$  only when estimating the backgroud in the data.

Backgroud determined with the described method is shown in Fig. 5.1 with the solid lines colored according to corresponding markers. This backgroud was subtracted and final, background-free distributions of the secondary vertex positions in the transverse and longitudinal direction are presented in Fig. 5.8. Most relevant region - the HFT detector extending between  $\sim 2$  cm and  $\sim 30$  cm is satisfactorily well described by MC. Also, the inner wall of the TPC at  $\sim 48$  cm well matches between data and MC.

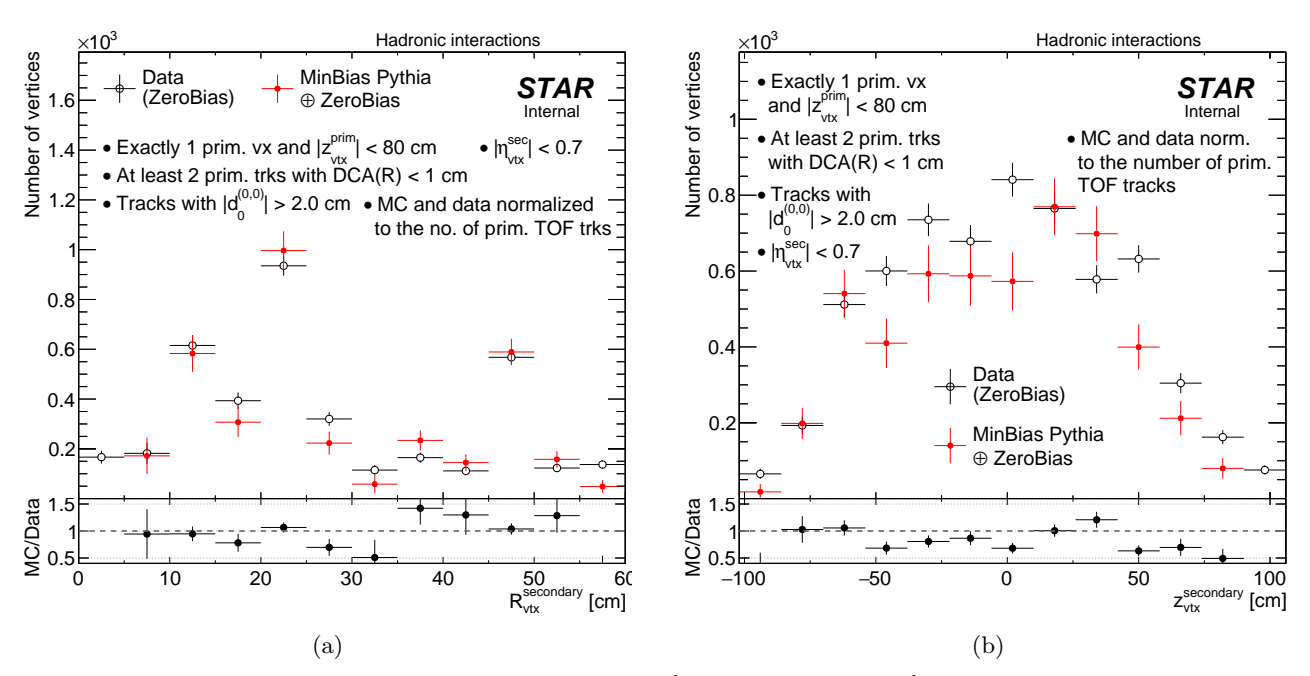


Figure 5.8: Comparison of background-subtracted  $R_{\rm vtx}^{\rm secondary}$  (5.8a) and  $z_{\rm vtx}^{\rm secondary}$  (5.8b) distribution in the data (opened black circles) and embedded MC (filled red circles). Only vertices recognized as products of hadronic interactions are shown in the figure.

# 6. Systematic errors

# List of Figures

1.1	TPC acceptance and reconstruction efficiency of $\pi^-$	4
1.2	TPC acceptance and reconstruction efficiency of $\pi^+$	6
1.3	TPC acceptance and reconstruction efficiency of $K^-$	8
1.4	TPC acceptance and reconstruction efficiency of $K^+$	10
1.5	TPC acceptance and reconstruction efficiency of $\bar{p}$	12
1.6	TPC acceptance and reconstruction efficiency of $p$	14
1.7	TOF acceptance, reconstruction and matching efficiency of $\pi^-$	17
1.8	TOF acceptance, reconstruction and matching efficiency of $\pi^+$	19
1.9	TOF acceptance, reconstruction and matching efficiency of $K^-$	21
	TOF acceptance, reconstruction and matching efficiency of $K^+$	23
		25
1.12	TOF acceptance, reconstruction and matching efficiency of $p$	27
3.1	Fits to dE/dx spectra from the data	32
3.2	Parameters of track $dE/dx$ as a function of reconstructed momentum for a few particle species	33
3.3	Comparison of dE/dx spectra between data and MC	34
4.1	Sketch of helix modification procedure and $d_0$ calculation	35
4.2	Example of comparison of $d_0$ histograms in the data and embedded MC in the procedure of TPC	
	pointing resolution adjustment	36
4.3	Example of $-\chi^2/\text{NDF}$ map in a parameter space in the procedure of TPC pointing resolution adjustment	36
4.4	Best-fit parameters obtained in the procedure of the TPC track pointing resolution adjustment.	$\frac{30}{36}$
4.5	Comparison of distribution of pion $d_0$ and components of DCA vector in the data and embedded	30
4.0	MC, before and after adjustment of TPC pointing resolution	37
5.1	Comparison of primary track multiplicity, $p_T$ and $\eta$ distribution in zero-bias data and embedded	
0.1	MC (minimum-bias)	38
5.2	Comparison of $d_0^{(0,0)}$ distribution of global TPC tracks matched with TOF in zero-bias data and	
	embedded MC (minimum-bias)	39
5.3	Multiplicity of tracks in reconstructed secondary vertices	40
5.4	$\eta_{\text{vtx}}$ definition (sketch)	40
5.5	$\eta_{ m vtx}$ definition (sketch)	41
5.6	Comparison of DCA between all pairs of secondary track candidates selected for the secondary	
	vertex reconstruction in the data and embedded MC	41
5.7	Comparison of radial DCA of all primary tracks matched with TOF and passing quality criteria	
	in events selected for secondary vertex analysis, between the data and embedded MC Comparison of background-subtracted $R_{\rm vtx}^{\rm secondary}$ and $z_{\rm vtx}^{\rm secondary}$ distribution in the data and em-	41
5.8	Comparison of background-subtracted $R_{\text{vtx}}^{\text{secondary}}$ and $z_{\text{vtx}}^{\text{secondary}}$ distribution in the data and em-	
	bedded MC	42

## List of Tables

3.1	Parameters of func	tions from Fig. 3	3.2 describing track	dE/dx as a	function of reconstructed	
	momentum for a fev	w particle species	(STARsim MC)			32

#### References

- $[1] \ \texttt{https://github.com/rafalsikora/CEP-STAR-AnalysisNote/blob/master/CEP\_AnalysisNote.pdf}.$
- [2] http://home.agh.edu.pl/~fulek/PID\_AnalysisNote.pdf.
- [3] https://www.star.bnl.gov/rt3/SelfService/Display.html?id=3272.
- [4] S. Das, "A simple alternative to the Crystal Ball function," arXiv:1603.08591 [hep-ex].
- [5] https://www.star.bnl.gov/rt3/SelfService/Display.html?id=3332.
- [6] https://online.star.bnl.gov/rp/pp200/.
- [7] https: //drupal.star.bnl.gov/STAR/system/files/LFSUPC\_PWGMeeting\_RafalSikora\_23April2018.pdf.